

Saturable Purcell filter for circuit quantum electrodynamics

Ivan Yakoupov  and Kazuki Koshino ^{*}

College of Liberal Arts and Sciences, Tokyo Medical and Dental University, 2-8-30 Konodai, Ichikawa, Chiba 272-0827, Japan

 (Received 15 February 2022; revised 16 January 2023; accepted 10 February 2023; published 27 February 2023)

We consider a typical circuit QED setup where an artificial atom encodes a qubit and is dispersively coupled to a measurement resonator that in turn is coupled to a transmission line. We show theoretically that by placing another artificial atom in this transmission line to act as a filter, the Purcell decay of the qubit into the transmission line is suppressed. When strong control fields are applied in the transmission line, the filter is saturated and effectively switched off. Such a Purcell filtering capability permits both the control and measurement of the qubit using the single transmission line, while maintaining the long coherence time of the qubit in the absence of the control pulses. We show that high fidelity Pauli σ_x gates on the qubit can be realized using simple pulse shapes. For devices that already use one transmission line both for control and measurement of the qubit, our paper provides a way to completely filter out the qubit frequency without removing the possibility of controlling the system. Further, combining the proposed filter with frequency multiplexing potentially enables both control and measurement of several qubits using a single Purcell-filtered transmission line. This will enhance the scalability of superconducting quantum processors by decreasing the number of the required transmission lines.

DOI: [10.1103/PhysRevResearch.5.013148](https://doi.org/10.1103/PhysRevResearch.5.013148)

I. INTRODUCTION

Superconducting quantum processors with moderate numbers of qubits are already available [1–5]. Error correction, where multiple physical qubits act as one logical qubit, is already being explored on such scalable hardware [6–8]. This means, however, that the number of the physical qubits has to increase drastically to be able to run useful quantum algorithms on the logical qubits. To do this, every part of the current setups needs to be improved: the artificial atoms that encode the qubits, the room-temperature electronics that controls them, and the interconnect. Simplifying the interconnect is the focus of this article. In particular, we will show how to reduce the number of the microwave transmission lines. The current approach is to use frequency multiplexing where several qubits are measured using the same transmission line [1–5]. Each qubit is coupled to the measurement line through a resonator that has a significantly different frequency. The measurement line is filtered to suppress the qubit decay into it. Such decay is conventionally called “Purcell decay” [9], and the filters are called “Purcell filters”.

The Purcell filters are designed to break the trade-off between fast measurement and small Purcell decay. This is done by filtering the frequencies close to the qubit transitions, but not the resonator frequencies [9–12] [see Figs. 1(a) and 1(b)]. Addition of an unsaturable Purcell filter to a transmission line

makes it more challenging to control the qubits, precisely due to the fact that the qubit frequencies are filtered out. If they are filtered out completely, a separate (unfiltered) control line is required for each qubit [1–5]. However, it is possible to make a trade-off between filtering and leaving a small coupling to perform control using the measurement line [12].

The qubit transition frequencies could not be filtered out completely before the introduction of the Josephson quantum filter (JQF) [13,14], which is another artificial atom. The JQF matches the qubit transition (i.e., the transition frequency of the two lowest energy levels the JQF is approximately the same as the qubit transition), is strongly coupled to the control line, and is placed half a wavelength apart as shown in Fig. 1(c). When a strong control pulse is applied, the JQF becomes saturated and effectively switched off. In the absence of the control pulses, the JQF prevents the decay of the qubit into the control line. Therefore, the JQF breaks the trade-off between fast control and small decay rate of the qubit into the control line.

In this article, we show that the JQF can also act as a Purcell filter when placed in the measurement line. Because the JQF can be saturated, it allows resonant control pulses to be sent in the measurement line, making the separate control lines unnecessary. This results in the setup shown in Fig. 1(d). We verify that simple control pulses are sufficient to implement high-fidelity gates on the qubit, and that the gate fidelity can be further increased using quantum optimal control. We also briefly comment on the combination of the JQFs with the frequency multiplexing. Such a combination would have the same low number of transmission lines as in Refs. [15–17], but with the Purcell filtering of the qubits. We expect that the Purcell filtering using a JQF will also be useful outside of the quantum computation context, e.g., in the hybrid systems setup of Ref. [18].

^{*}kazuki.koshino@osamember.org

Published by the American Physical Society under the terms of the Creative Commons Attribution 4.0 International license. Further distribution of this work must maintain attribution to the author(s) and the published article's title, journal citation, and DOI.

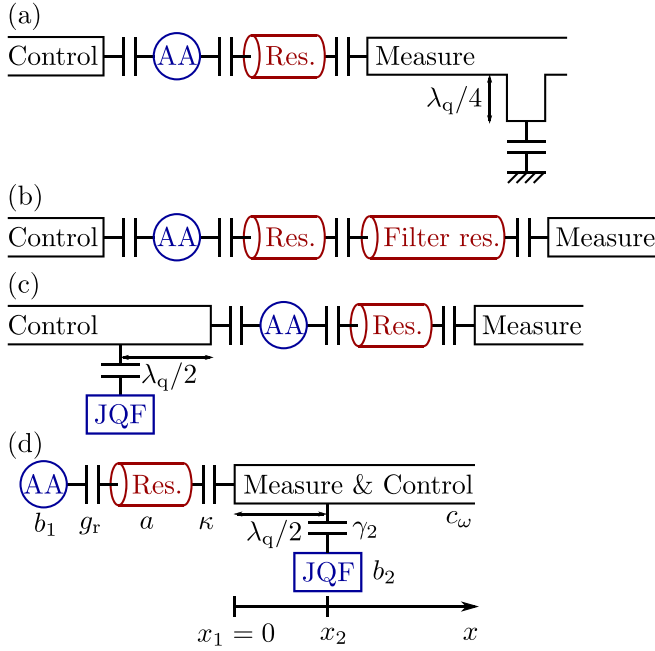


FIG. 1. (a) Band-rejection Purcell filtering using a stub filter [9]. The qubit is encoded in the coupled eigenstates (dressed states) of an artificial atom (AA) and a resonator (Res.). The measurement line is connected to the resonator and has an open circuit stub with length $\lambda_q/4$, where λ_q is the wavelength corresponding to the qubit transition. Alternative designs of the band-rejection filters can be found in Refs. [11,12]. (b) Bandpass Purcell filtering using a filter resonator [10]. The frequencies of the resonators are the same or close to each other. (c) Filtering of the control line using a Josephson quantum filter (JQF) [13,14] placed $\lambda_q/2$ away from the qubit. The Purcell filter in the measurement line is not shown. (d) The setup that we consider—JQF as a saturable Purcell filter in the combined measurement and control line.

The rest of the article is organized as follows. In Sec. II we describe our theoretical model and its associated parameters. In Sec. III, we show that the Purcell decay is suppressed by the JQF. In Sec. IV, we show that the JQF does not disturb the measurement of the qubit. In Sec. V, we show that the qubit can be controlled despite the presence of the JQF by finding the pulse shapes that implement a high-fidelity Pauli σ_x gate. The article is concluded by Sec. VI.

II. SETUP

We assume transmons, modeled as anharmonic oscillators, for the artificial atoms. Using the two-level atoms gives similar results [13,14]. The considered setup is shown in Fig. 1(d). One transmon is coupled to a transmission line through a resonator. The subsystem consisting of this transmon and resonator has index 1 in the equations below and encodes a qubit in its coupled eigenstates (dressed states). The subsystem 2 is a transmon that is coupled to the same line directly and is used as a JQF. The JQF is placed $\lambda_q/2$ from the resonator, where λ_q is the wavelength that corresponds to the qubit transition frequency. The Hamiltonian of the setup can be written $H = H_s + H_f + H_i$. The parts H_s , H_f , and H_i correspond to

the system, transmission line field, and the interaction, respectively.

The system part is $H_s = \sum_{m=1}^2 H_{s,m}$, where the subsystem 1 part is

$$H_{s,1} = \hbar\omega_{t,1}b_1^\dagger b_1 + \hbar\frac{\alpha_1}{2}(b_1^\dagger)^2 b_1^2 + \hbar\omega_t a^\dagger a + \hbar g_t (b_1^\dagger a + a^\dagger b_1), \quad (1)$$

and the subsystem 2 part is

$$H_{s,2} = \hbar\omega_{t,2}b_2^\dagger b_2 + \hbar\frac{\alpha_2}{2}(b_2^\dagger)^2 b_2^2. \quad (2)$$

The resonator has the corresponding annihilation operator a and the frequency ω_t . There are 2 transmons with the corresponding annihilation operators b_m , transition frequencies $\omega_{t,m}$ of the lowest two energy levels, and the anharmonicity parameters α_m . Only the transmon with the index $m = 1$ is coupled to the resonator with the coupling strength g_t .

Multiple resonator modes could have a significant contribution to the Purcell decay [18,19]. This occurs when the detunings of several modes of the resonator from the qubit frequency have similar magnitudes. It is possible to model a multimode resonator as several single-mode ones [20–22], but for simplicity, we only consider the parameter regime where one of the resonator modes is dominant. We use the parameters close to Ref. [14], where a coplanar waveguide resonator with the fundamental frequency $\omega_t/(2\pi) = 10$ GHz was coupled to the transmon with the transition frequency $\omega_{t,1}/(2\pi) = 8$ GHz. The next mode of the resonator has the frequency $2\omega_t/(2\pi) = 20$ GHz, and hence does not contribute much to the Purcell decay.

The existence of the higher modes does not significantly change the required JQF parameters. The JQF needs to have the frequency close to the qubit frequency, not the resonator modes. The resonator modes shift the qubit frequency due to the coupling, but the shift due to the fundamental mode is a few MHz for the considered parameters, and the shift due to the higher modes is even smaller. In practice, the frequency of the JQF may need to be tuned post fabrication anyway, either using the bias flux [14] or the laser annealing [5]. Hence, even the predictions of a single-mode theory should be sufficient for this parameter regime.

The transmission line field part is

$$H_f = \hbar \int_0^\infty \omega c_\omega^\dagger c_\omega d\omega. \quad (3)$$

The annihilation operators c_ω correspond to the modes $\cos(k_\omega x)$ with positive wave vectors k_ω , but use the angular frequencies ω as the integration variable. The dispersion relation is $\omega = k_\omega v_g$, with v_g being the speed of light (group velocity) in the transmission line.

The interaction part is

$$H_i = -\hbar \sum_{m=1}^2 \int_0^\infty g_m(\omega)(c_\omega - c_\omega^\dagger)(\mathcal{O}_m - \mathcal{O}_m^\dagger)d\omega, \quad (4)$$

where $g_m(\omega) = G_m\sqrt{\omega} \cos(k_\omega x_m)$, $G_m = \sqrt{\Gamma_m/(2\pi\omega_m)}$,

$$\Gamma_m = \begin{cases} \kappa & \text{for } m = 1, \\ \gamma_2 & \text{for } m = 2, \end{cases} \quad (5)$$

$$\omega_m = \begin{cases} \omega_r & \text{for } m = 1, \\ \omega_{t,2} & \text{for } m = 2, \end{cases} \quad (6)$$

$$\mathcal{O}_m = \begin{cases} a & \text{for } m = 1, \\ b_2 & \text{for } m = 2. \end{cases} \quad (7)$$

The interaction Hamiltonian (4) gives rise to the decay rates κ (resonator) and γ_2 (JQF). We use the coupling of the form $g_m(\omega) = G_m\sqrt{\omega} \cos(k_\omega x_m)$, which is obtained by ignoring the so-called A^2 term. A more careful derivation [20–23] results in $g_m(\omega) = G_m(\sqrt{\omega}/\sqrt{1 + \mathcal{A}\omega^2}) \cos(k_\omega x_m)$, i.e., has a cutoff for the higher ω controlled by the parameter $\mathcal{A} > 0$. The form of g_m with the cutoff results in the renormalization of the decay rates and an additional collective frequency shift as detailed in Appendix B. The theoretical model without a cutoff, i.e., with $g_m(\omega) = G_m\sqrt{\omega} \cos(k_\omega x_m)$, was found to be in good agreement with the experiment when the JQF was placed in the dedicated control line [14], suggesting that the influence of the additional frequency shift is small. To estimate its effect theoretically, the numerical value of \mathcal{A} is needed, and it does not seem to be available in the literature. Due to these considerations, we proceed with $g_m(\omega) = G_m\sqrt{\omega} \cos(k_\omega x_m)$, but the calculations could be easily adjusted for a nonzero \mathcal{A} .

The constants G_m could also be related to the circuit parameters, but we write them in terms of the decay rates Γ_m , which can be measured experimentally [14]. If the A^2 terms are included, these constants could be modified to $G_m = \sqrt{\Gamma_m(1 + \mathcal{A}\omega_m^2)/(2\pi\omega_m)}$ to account for the renormalization. Another note is that the rotating wave approximation is not applied immediately in H_i . It will be applied after the effective Heisenberg equations of motion for the subsystems are obtained to ensure that all the terms are present [24]. More details about this can be found in Appendices A and B where the master equation is derived starting from the Hamiltonian above and following Refs. [13,14,24,25]. Here, we only give the outline of this derivation.

In general, the interaction of matter with the electromagnetic fields results in non-Markovian equations of motion [26,27] caused by the fact that it takes a finite time for the photons to propagate between the atoms. For $g_m(\omega) = G_m\sqrt{\omega} \cos(k_\omega x_m)$, the effective equations of motion where the field degrees of freedom are traced out, take the form of the delay differential equations. However, the delay differential equations are difficult to solve in the general case, and hence some kind of approximation is usually needed. We adopt the approximation that converts the time delays into the propagation phase factors [13,14,24,25]. For $g_m(\omega) = G_m(\sqrt{\omega}/\sqrt{1 + \mathcal{A}\omega^2}) \cos(k_\omega x_m)$, the equations of motion are of a more general form with a memory kernel given by Eq. (A9) in Appendix A. This case can also be approximated by a Markovian master equation as explained in Appendix B.

Before we explain the approximation involved in replacing the non-Markovian equations of motion with the Markovian ones, we first note that we diagonalize the subsystem Hamiltonians $H_{s,m}$. For every pair of eigenstates $|j_m\rangle, |j'_m\rangle$ of $H_{s,m}$, we define the operators $\sigma_{m,jj'} = |j_m\rangle\langle j'_m|$ and the matrix elements

$C_{m,jj'} = \langle j_m|\mathcal{O}_m|j'_m\rangle$. We order the eigenstates such that the number of excitations increases or is constant with increasing j . Since \mathcal{O}_m is an annihilation operator, the rotating wave approximation ensures that $C_{m,jj'} \neq 0$ only for $j < j'$. We can write

$$H_{s,m} = \hbar \sum_j \omega_{m,j} \sigma_{m,jj}, \quad (8)$$

where $\omega_{m,j}$ are the eigenfrequencies.

Assuming that the Hamiltonian is dominated by the system parts (8), the approximation of the time-delayed terms can be written

$$\sigma_{m,jj'}(t - t_x) \approx \sigma_{m,jj'}(t) e^{i(\omega_{m,j'} - \omega_{m,j})t_x}, \quad (9)$$

making the Heisenberg equations of motion for the attached subsystems local in time. When a classical drive with frequency ω_d is present, we make the approximation

$$\sigma_{m,jj'}(t - t_x) \approx \sigma_{m,jj'}(t) e^{i\omega_d t_x} \quad (10)$$

instead. Physically, this means that the driven subsystems oscillate with the drive frequency rather than their eigenfrequencies.

The derivation assumes a coherent state with the carrier frequency ω_d as the input in the transmission line, and hence an additional drive Hamiltonian

$$H_d = \hbar \sum_{m=1}^2 (\Omega_m e^{-i\omega_d t} \mathcal{O}_m^\dagger + (\Omega_m)^* e^{i\omega_d t} \mathcal{O}_m) \quad (11)$$

emerges with the Rabi frequencies

$$\Omega_m = \sqrt{\frac{\omega_d}{\omega_m}} \Gamma_m \hbar \cos(k_{\omega_d} x_m) e^{i\phi}, \quad (12)$$

which may be time-dependent due to the changing photon flux \dot{n} and phase ϕ .

The rotating frame is defined with respect to the Hamiltonian

$$H_0 = \hbar \sum_{m=1}^2 \sum_j \omega_{0,m,j} \sigma_{m,jj}, \quad (13)$$

where the frequencies $\omega_{0,m,j}$ are chosen such that the factors $e^{\pm i\omega_d t}$ in Eq. (11) are canceled, i.e., $\frac{i}{\hbar}[H_0, \mathcal{O}_m] = -i\omega_d \mathcal{O}_m$. If there is no drive, any fixed frequency can be used instead of ω_d . The Hamiltonian in the rotating frame is

$$\begin{aligned} \tilde{H} = \hbar \sum_{m=1}^2 \sum_j (\omega_{m,j} - \omega_{0,m,j}) \sigma_{m,jj} \\ + \text{Re}[\Omega] \tilde{H}_{d,\text{Re}} + \text{Im}[\Omega] \tilde{H}_{d,\text{Im}}, \end{aligned} \quad (14)$$

where we have picked $\Omega = \Omega_1$ as the reference Rabi frequency. Defining

$$\tilde{\Omega}_m = \frac{\text{Re}[\Omega_m]}{\text{Re}[\Omega]} = \frac{\text{Im}[\Omega_m]}{\text{Im}[\Omega]} = \sqrt{\frac{\omega_{m_0}}{\omega_m} \frac{\Gamma_m}{\Gamma_{m_0}} \frac{\cos(k_{\omega_d} x_m)}{\cos(k_{\omega_d} x_{m_0})}}, \quad (15)$$

we can write

$$\tilde{H}_{d,\text{Re}} = \hbar \sum_{m=1}^2 \tilde{\Omega}_m (\mathcal{O}_m^\dagger + \mathcal{O}_m), \quad (16a)$$

$$\tilde{H}_{d,\text{Im}} = i\hbar \sum_{m=1}^2 \tilde{\Omega}_m (\mathcal{O}_m^\dagger - \mathcal{O}_m). \quad (16b)$$

The ratios $\tilde{\Omega}_m$ do not depend on the photon flux \dot{n} or phase ϕ , and hence $\tilde{H}_{d,\text{Re}}$ and $\tilde{H}_{d,\text{Im}}$ are independent of time. The time dependence of \tilde{H} is contained in the factors $\text{Re}[\Omega]$ and $\text{Im}[\Omega]$.

The master equation can be written

$$\begin{aligned} \dot{\tilde{\rho}}_s &= \mathcal{L}(\tilde{\rho}_s) \\ &= -\frac{i}{\hbar} [\tilde{H}, \tilde{\rho}_s] + \frac{1}{2} \sum_{m,n=1}^2 (\mathcal{O}_{mn} \tilde{\rho}_s \mathcal{O}_m^\dagger - \mathcal{O}_m^\dagger \mathcal{O}_{mn} \tilde{\rho}_s) \\ &\quad + \frac{1}{2} \sum_{m,n=1}^2 (\mathcal{O}_n \tilde{\rho}_s \mathcal{O}_{nm}^\dagger - \tilde{\rho}_s \mathcal{O}_{nm}^\dagger \mathcal{O}_n), \end{aligned} \quad (17)$$

where $\mathcal{O}_{mn} = \sum_{j,j'} \xi_{mn,j'j} \mathcal{C}_{n,jj'} \sigma_{n,jj'}$,

$$\begin{aligned} \xi_{mn,j'j} &= \frac{\sqrt{\Gamma_m \Gamma_n}}{2} \frac{\omega_{n,j'j}}{\sqrt{\omega_m \omega_n}} \\ &\quad \times (e^{ik_{n,j'j} x_m - x_n} + e^{ik_{n,j'j} x_m + x_n}), \end{aligned} \quad (18)$$

$\omega_{n,j'j} = \omega_{n,j'} - \omega_{n,j}$ are the transition frequencies between the eigenstates j and j' , $k_{n,j'j} = k_{\omega_{n,j'j}}$ are the corresponding wavevectors, and $\tilde{\rho}_s = e^{iH_0 t/\hbar} \text{tr}[\rho] e^{-iH_0 t/\hbar}$ is the density matrix with the transmission line field degrees of freedom traced out, in the rotating frame with respect to the Hamiltonian (13). If a classical drive is present, we set $k_{n,j'j} = k_{\omega_d}$ in Eq. (18), while keeping the factor $\omega_{n,j'j}/\sqrt{\omega_m \omega_n}$ unchanged. For $g_m(\omega) = G_m(\sqrt{\omega}/\sqrt{1+\mathcal{A}\omega^2}) \cos(k_\omega x_m)$ with $\mathcal{A} > 0$, $\xi_{mn,j'j}$ is given by Eq. (B16) derived in Appendix B instead of Eq. (18).

The Schrieffer-Wolff transformation on the Hamiltonian (1) results in the dispersive shifts for every transmon energy level [28]. We define

$$\chi = \frac{g_r^2}{2(\omega_r - \omega_{t,1})} \left(1 - \frac{\omega_r - \omega_{t,1} + \alpha_1}{\omega_r - \omega_{t,1} - \alpha_1} \right) \quad (19)$$

in terms of the difference of the dispersive shifts for the lowest two levels. For $\alpha_1 \rightarrow \infty$, this reduces to the two-level system shift $\chi = g_r^2/(\omega_r - \omega_{t,1})$.

For the calculations below, the parameters are chosen close to the ones in Ref. [14]. We set the frequency of the resonator $\omega_r/(2\pi) = 10$ GHz, resonator decay rate $\kappa/(2\pi) = 2$ MHz, transition frequencies of the lowest two transmon energy levels $\omega_{t,1}/(2\pi) = 8.000$ GHz and $\omega_{t,2}/(2\pi) = 7.994$ GHz (shifted to match the qubit transition frequency $\omega_{1,10}/(2\pi)$), anharmonicities $\alpha_1/(2\pi) = \alpha_2/(2\pi) = -400$ MHz, JQF decay rate $\gamma_2/(2\pi) = 100$ MHz, and the dispersive shift $\chi/(2\pi) = 1$ MHz. From Eq. (19), the coupling between the transmon and the resonator is $g_r/(2\pi) = 109.544$ MHz. The resonator is placed at the origin, $x_1 = 0$, and the JQF is placed half a wavelength from the resonator, $k_{\omega_{1,10}} x_2 = \pi$. We also choose $\Omega = \Omega_1$ as the reference Rabi frequency, and hence $\tilde{\Omega}_1 = 1$ and $\tilde{\Omega}_2 = \sqrt{\omega_r \gamma_2/(\omega_{t,2} \kappa)} \cos(k_{\omega_d} x_2)$.

As explained above, the Hamiltonian (1) for the subsystem 1 is written in the diagonal form (8) prior to the derivation of the master equation (17) (the Hamiltonian (2) for the subsystem 2 is already diagonal). Truncated to at most one excitation either in the transmon or the resonator, we can write the Hamiltonian (1) as the matrix

$$\begin{pmatrix} 0 & 0 & 0 \\ 0 & \omega_r & g_r \\ 0 & g_r & \omega_{t,1} \end{pmatrix}, \quad (20)$$

where the zero row and column were added explicitly for the zero-excitation state $|0_1\rangle$. This is also one of the eigenstates of the matrix. The other two eigenstates have a single excitation and can be written

$$|1_1\rangle = \sin(\theta) a^\dagger |0_1\rangle - \cos(\theta) b_1^\dagger |0_1\rangle, \quad (21a)$$

$$|2_1\rangle = \cos(\theta) a^\dagger |0_1\rangle + \sin(\theta) b_1^\dagger |0_1\rangle, \quad (21b)$$

where $\theta = \frac{1}{2} \arg[(\omega_r - \omega_{t,1})/2 + ig_r]$, and \arg is the argument of a complex number. Below, we use the computational basis states $|0\rangle = |0_1\rangle$ and $|1\rangle = |1_1\rangle$. The state $|2_1\rangle$ is the rapidly-decaying eigenstate with most of the excitation in the resonator, and is outside of the computational basis. The corresponding eigenfrequencies are $\omega_{1,0} = 0$,

$$\omega_{1,1} = \frac{\omega_r + \omega_{t,1}}{2} - \sqrt{\left(\frac{\omega_r - \omega_{t,1}}{2}\right)^2 + g_r^2}, \quad (22a)$$

$$\omega_{1,2} = \frac{\omega_r + \omega_{t,1}}{2} + \sqrt{\left(\frac{\omega_r - \omega_{t,1}}{2}\right)^2 + g_r^2}. \quad (22b)$$

With the chosen parameters above, we have $\omega_{1,1}/(2\pi) = 7.994$ GHz and $\omega_{1,2}/(2\pi) = 10.006$ GHz.

The single-excitation states are sufficient to describe the decay in Sec. III below. The measurement (Sec. IV) and control (Sec. V) involves sending microwave fields through the transmission line and hence can excite the higher eigenstates. In the general case, we truncate the transmons and the resonator at a certain maximal number of excitations and then perform the numerical diagonalization of the resulting Hamiltonian matrices. This produces an eigenfrequency $\omega_{m,j}$ for each eigenstate $|j_m\rangle$. Physically, only the transition frequencies $\omega_{m,j'j} = \omega_{m,j'} - \omega_{m,j}$ are relevant. However, the choice $\omega_{1,0} = 0$ as the frequency of the zero-excitation eigenstate $|0_1\rangle$ results in the identities $\omega_{1,10} = \omega_{1,1}$ and $\omega_{1,20} = \omega_{1,2}$. Hence, for the single-excitation states, the distinction between the absolute eigenfrequencies and the transition frequencies does not exist. This distinction becomes important for the higher-excitation states.

For example, the JQF transmon is described by an anharmonic ladder of eigenstates, as shown in Fig. 2(b). The states up to two excitations are $|0_2\rangle$, $|1_2\rangle$, and $|2_2\rangle$. The corresponding absolute eigenfrequencies are $\omega_{2,0} = 0$, $\omega_{2,1}/(2\pi) = 7.994$ GHz, and $\omega_{2,2}/(2\pi) = 15.588$ GHz. The transition frequencies are $\omega_{2,10}/(2\pi) = 7.994$ GHz and $\omega_{2,21}/(2\pi) = 7.594$ GHz. These are the only transitions that have the nonzero matrix elements $C_{2,jj'} = \langle j_2 | \mathcal{O}_2 | j_2' \rangle = \langle j_2 | b_2 | j_2' \rangle$ in the two-excitation subspace. When diagonalizing the transmon and resonator subsystem, the nonzero matrix elements $C_{1,jj'} = \langle j_1 | \mathcal{O}_1 | j_1' \rangle = \langle j_1 | a | j_1' \rangle$ have a more compli-

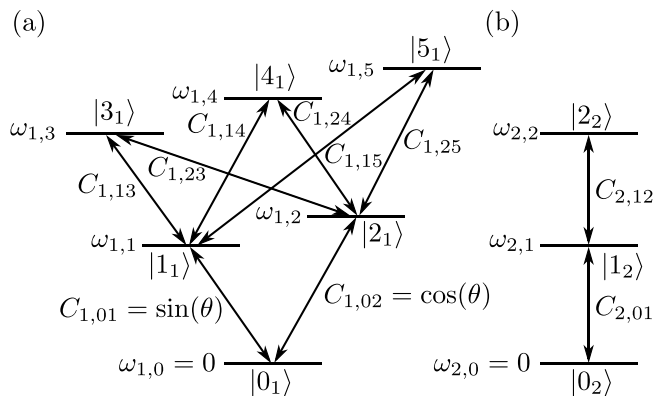


FIG. 2. (a) The level diagram of the coupled transmon and resonator subsystem, showing the eigenstates (dressed states) $|j_1\rangle$ up to two excitations with the corresponding eigenfrequencies $\omega_{1,j}$. The qubit is encoded in the states $|0_1\rangle$ and $|1_1\rangle$. For $\omega_{1,1}$ and $\omega_{1,2}$, there are analytical expressions [cf. Eqs. (22)]. The nonzero matrix elements $C_{1,jj'} = \langle j_1 | \mathcal{O}_1 | j_1' \rangle = \langle j_1 | a | j_1' \rangle$ are shown as lines with arrows between the eigenstates. For $C_{1,01}$ and $C_{1,02}$, there are analytical expressions using Eqs. (21). (b) The level diagram of the transmon JQF subsystem, showing the eigenstates $|j_2\rangle$ up to two excitations. Since the Hamiltonian (2) is already diagonal, the eigenfrequencies are linear combinations of its parameters: $\omega_{2,1} = \omega_{t,2}$, $\omega_{2,2} = 2\omega_{t,2} + \alpha_2$. The shown nonzero matrix elements $C_{2,jj'} = \langle j_2 | \mathcal{O}_2 | j_2' \rangle = \langle j_2 | b_2 | j_2' \rangle$ are $C_{2,01} = 1$ and $C_{2,12} = \sqrt{2}$.

cated structure, as shown in Fig. 2(a). Hence more transition frequencies $\omega_{m,j'j}$ are relevant to the dynamics.

III. SUPPRESSED PURCELL DECAY

First, we verify that the decay of a qubit is reduced by adding a JQF. The computational basis state $|0\rangle = |0_1\rangle$ is the zero-excitation state and hence does not decay. The decay of the state $|1\rangle = |1_1\rangle$ [cf. Eq. (21a)] is suppressed by the large detuning of the resonator even without a JQF. From the master equation (17), the Purcell decay rate is

$$\kappa_{\text{Purcell}} = |C_{1,01}|^2 \xi_{1,1,10} = \sin^2(\theta) \kappa \frac{\omega_{1,10}}{\omega_r}, \quad (23)$$

where $\omega_{1,10} = \omega_{1,1} - \omega_{1,0}$, $\omega_{1,1}$ is given by Eq. (22a), and $\omega_{1,0} = 0$. Since the detuning $\omega_r - \omega_{t,1}$ is large, we can approximate $\sin^2(\theta) \approx (g_r/(\omega_r - \omega_{t,1}))^2$, resulting in $\kappa_{\text{Purcell}} \approx (g_r/(\omega_r - \omega_{t,1}))^2 \kappa \omega_{1,10}/\omega_r$. The only difference from the usual formula for the Purcell decay rate is an additional factor $\omega_{1,10}/\omega_r$. This factor comes from the definition of the frequency-dependent coupling $g_1(\omega) = \sqrt{\kappa}/(2\pi\omega_r) \sqrt{\omega} \cos(k_\omega x_1)$ that results in the decay rate κ of the resonator with the frequency ω_r that is not coupled to the transmon and placed such that $\cos(k_\omega x_1) = 1$. The qubit transition frequency $\omega_{1,10}$ is different, and hence the decay rate that is proportional to $g_1^2(\omega_{1,10})$ gets this additional factor $\omega_{1,10}/\omega_r$. For our parameters, $\omega_{1,10}/\omega_r = 0.7994$, and $\kappa_{\text{Purcell}}/(2\pi) = 4.8$ kHz.

A Purcell filter needs to suppress the decay rate below κ_{Purcell} . We show in Fig. 3 that addition of a JQF accomplishes this. We initialize the qubit in the state $|1\rangle = |1_1\rangle$, and the JQF (if present) is initialized in its ground state $|0_2\rangle$. The error

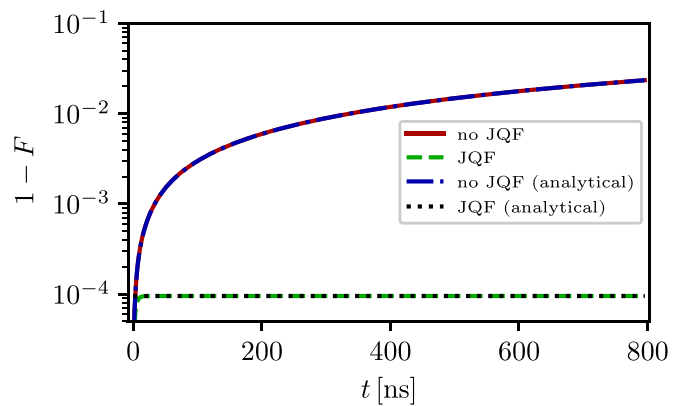


FIG. 3. The error probability $1 - F$ where F is given by Eq. (24) as a function of time for the qubit initialized in the state $|1\rangle = |1_1\rangle$ [cf. Eq. (21a)], and the JQF initialized in the ground state $|0_2\rangle$. The dash-dotted-blue curve plots $1 - e^{-\kappa_{\text{Purcell}} t}$ with κ_{Purcell} given by Eq. (23). The horizontal-dotted-black line plots $1 - F_{\text{dark}}$ given by Eq. (25). It overlaps the dashed-green curve for large times.

probability $1 - F$ is plotted, where the fidelity F is

$$F = \text{tr}_s[(\sigma_{1,11} \otimes I_2) \tilde{\rho}_s(t)], \quad (24)$$

and tr_s is the trace over the system degrees of freedom (the trace over the transmission line degrees of freedom tr_f has already been performed during the derivation of the master equation in Appendix A). We have also written the tensor product with the identity operator I_2 on the subsystem 2 (JQF) in Eq. (24) explicitly, so that it is more easily seen that $F = \langle 1 | \text{tr}_2(\tilde{\rho}_s) | 1 \rangle$, where tr_2 is the trace over the subsystem 2.

The solid-red curve in Fig. 3 is the numerically calculated error probability $1 - F$ without a JQF, and the overlapping dash-dotted-blue curve plots $1 - e^{-\kappa_{\text{Purcell}} t}$. We see that the behavior of the dashed-green curve that shows the case with a JQF is qualitatively the same as when the JQF was placed in the dedicated control line [13,14]. The qubit and the JQF have a bright state that decays rapidly and a dark state that does not decay. The state $|1_1\rangle \otimes |0_2\rangle$ (the qubit is in state $|1\rangle$, and the JQF is in the ground state), has both bright and dark parts. Because the JQF decay rate γ_2 is significantly larger than κ_{Purcell} , this state is mostly dark. After the rapid decay of the small bright part, the decay rate vanishes. The fidelity after the bright part has decayed is

$$F_{\text{dark}} = \left(\frac{\gamma_2}{\kappa_{\text{Purcell}} + \gamma_2} \right)^2, \quad (25)$$

and $1 - F_{\text{dark}}$ is shown by the horizontal dotted black line in Fig. 3.

In practice, the decay rate is not expected to be zero due to the imperfections in the qubit and the JQF but still be reduced compared to the case without the JQF. We show the influence of some of the possible imperfections in Fig. 4. If the JQF transition frequency $\omega_{t,2}$ does not match the qubit transition frequency $\omega_{1,10}$, the decay rate is not canceled completely, as shown in Fig. 4(a). The cancellation is also imperfect if the JQF is not placed at $x_2 = \pi/k_{\omega_{1,10}}$, as shown in Fig. 4(b). The influence of the internal decay of the JQF with the rate $\gamma_{2,\text{int}}/(2\pi) = 3$ MHz [14] is

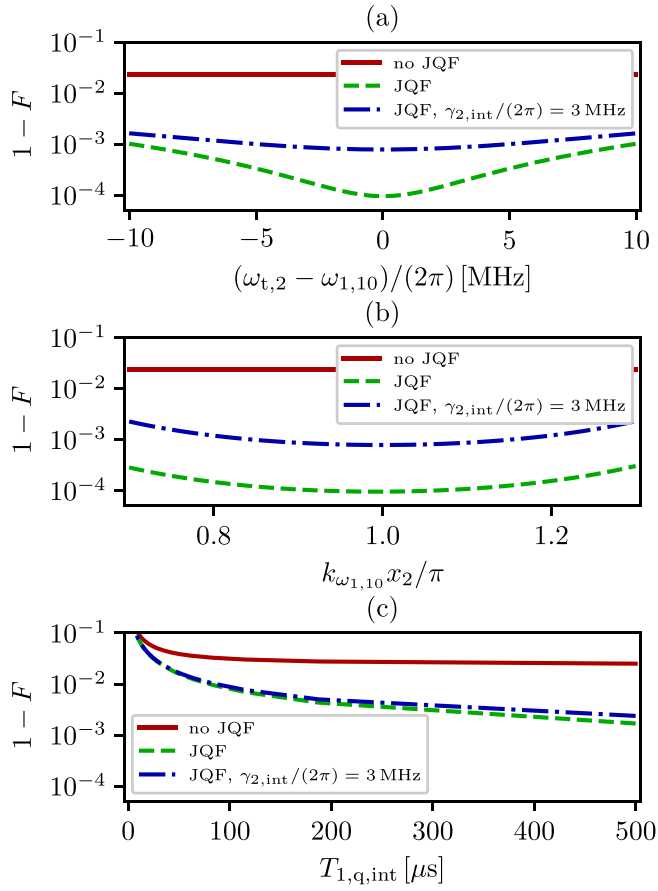


FIG. 4. The error probability $1 - F$ where F is given by Eq. (24) as a function of: (a) JQF transition frequency $\omega_{t,2}$, (b) JQF position x_2 , (c) internal T_1 time of qubit ($T_{1,q,int} = 1/\gamma_{q,int}$, where $\gamma_{q,int}$ is discussed in the text). In all the subplots, the qubit was initialized in the state $|1\rangle$ and evolved for the same time $t_f = 10/\kappa \approx 800$ ns as in Fig. 3, plotting the final value. For the solid-red and dashed-green curves, the parameters are the same as in Fig. 3, except for $\omega_{t,2}$ in (a), x_2 in (b), and $T_{1,q,int}$ in (c). The dash-dotted-blue curves show the influence of the internal decay of the JQF with the rate $\gamma_{2,int}/(2\pi) = 3$ MHz [14].

shown as the dash-dotted-blue curves in Fig. 4, calculated by phenomenologically adding a decay term $\gamma_{2,int}\mathcal{D}[b_2]\rho = (\gamma_{2,int}/2)(2b_2\rho b_2^\dagger - \rho b_2^\dagger b_2 - b_2^\dagger b_2\rho)$ to the master equation (17). An imperfect JQF provides a significant reduction of the Purcell decay, even if it does not make it vanish completely. The internal decay of the qubit is modeled by adding $\gamma_{q,int}\mathcal{D}[b_1]\rho$ to the master equation, and Fig. 4(c) shows the influence of the different $T_{1,q,int} = 1/\gamma_{q,int}$. Even for $T_{1,q,int} = 50$ μs [29], the difference in the error probability $1 - F$ is significant, becoming more than an order of magnitude for $T_{1,q,int} = 500$ μs [30,31]. These differences could be larger if the Purcell limited T_1 time, $1/\kappa_{\text{Purcell}} \approx 33$ μs , were lower, e.g., by choosing a smaller detuning $\omega_r - \omega_{t,1}$, which may decrease the gate time.

In Appendix C, we check the approximation (9) used in the derivation of the master equation (17) numerically. Without this approximation, delay differential equations are obtained, and they can be solved for the single-excitation subspace. The

differences between the two models can only be seen with significant zoom factors, with the $1 - F$ curves deviating on the order of 10^{-6} or less.

IV. MEASUREMENT

The dispersive shifts of the resonator frequency depend on the state of the transmon [28], and this is the standard physical mechanism for the qubit measurement in the superconducting quantum processors [1–5,10]. The desirable parameter regime is where the internal losses are negligible on the time scales of the duration of the measurement. Here, we only consider zero internal losses in the model, but these losses could be added as in the previous section. Since the considered setup [Fig. 1(d)] is in the reflection geometry and under the assumption of zero internal losses, all of the incident radiation gets reflected due to the energy conservation. Hence, no information can be gained from the amplitude of the reflected field, and only its phase carries the information about the qubit. The experimentally accessible I and Q values could be obtained by the phase-preserving amplification [32] and mixing with a local carrier on an IQ mixer [1]. Then the I and Q values are proportional to the sine and cosine of the reflected phase [33]. With the fast analog to digital converters [34,35], an IQ mixer may not be needed, and then the relationship between the reflected phase and the final processed values could in principle be arbitrary.

Since the JQF is far detuned from the probe (around 2 GHz in our assumed parameters), it is weakly excited even for moderate powers of the probing field. For example, the maximum JQF population $\langle b_2^\dagger b_2 \rangle$ for the parameters of Fig. 5 is around 3×10^{-4} . Therefore, the noise contribution is assumed to be negligible, and instead of the more advanced theoretical descriptions of the measurement mechanism that also include the noise contributions [36,37], we take the simple approach of only considering the expectation values of the complex reflection coefficient r . The optimal situation is when the reflection coefficients, interpreted as 2D vectors with the components $\text{Re}[r]$ and $\text{Im}[r]$, point in the opposite directions for the computational basis states $|0\rangle$ and $|1\rangle$ [38]. In the dispersive approximation, this gives the condition $\chi = \kappa/2$, so that the dispersive shift χ is large enough compared to the resonator linewidth κ to obtain the maximum angle of π between the reflection coefficients.

In Appendix D, we derive the expression for the reflection coefficient

$$r = 1 - i \sum_{m=1}^2 \sum_{j,j'} \frac{\omega_{m,j'j}}{\sqrt{\omega_1 \omega_m}} \frac{\sqrt{\Gamma_1 \Gamma_m}}{\Omega_1} C_{m,jj'} \times \text{tr}_s[\sigma_{m,jj'} \tilde{\rho}_s] \cos(k_{\omega_q} x_m) \quad (26)$$

at the position $x_2^+ = x_2 + \epsilon$ for $\epsilon \rightarrow 0$ from above, i.e., just to the right of the last subsystem attached to the transmission line (the JQF). The expression is written in terms of the reference Rabi frequency Ω_1 , and the overall propagation phase $e^{2ik_{\omega_q} x_2^+}$ has been removed. The master equation (17) is solved to evaluate the expectation values $\text{tr}_s[\sigma_{m,jj'} \tilde{\rho}_s]$, and the reflection coefficient as a function of time is calculated. The true steady-state reflection coefficient for both of the two

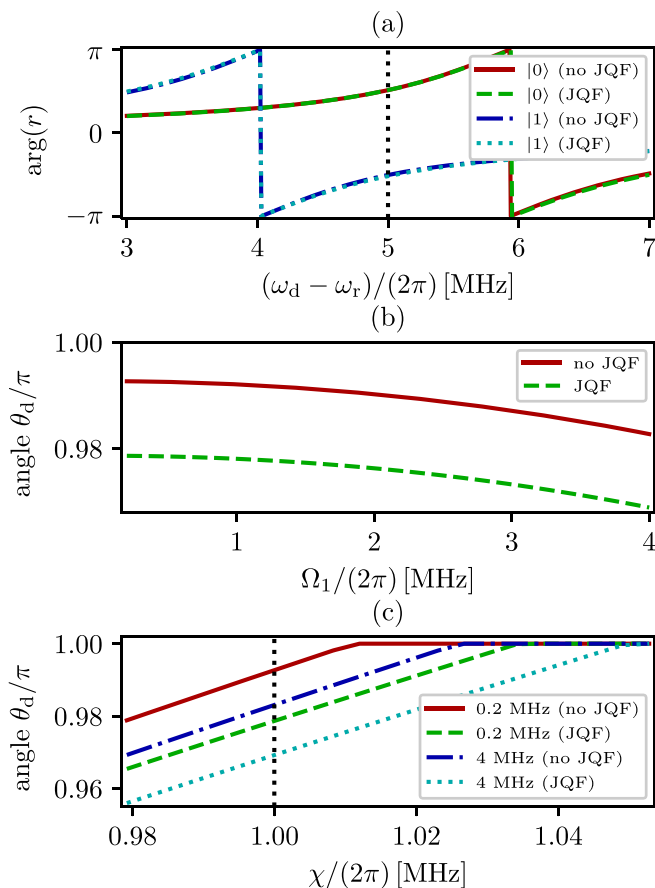


FIG. 5. (a) The phase of the reflection coefficient (26) as a function of the probe frequency ω_d for the Rabi frequency $\Omega_1/(2\pi) = 4$ MHz, corresponding to -125 dBm [cf. Eq. (12)] and 16 photons on average inside an empty resonator that is probed on resonance ($\omega_d = \omega_r$) without a JQF in front. In this and the other subfigures, the qubit is initialized either in the state $|0\rangle$ or the state $|1\rangle$ and evolved for a fixed time $t_f = 20/\kappa \approx 1.6 \mu\text{s}$. (b) The angle (27) between the states $|0\rangle$ and $|1\rangle$ as a function of the Rabi frequency Ω_1 at the probing frequency $(\omega_d - \omega_r)/(2\pi) = 5$ MHz [vertical-dotted-black line in (a)]. (c) The angle (27) as a function of the dispersive shift χ [related to the coupling g_r by Eq. (19)] for a probing frequency ω_d optimized numerically [39,40] to give the maximum angle. The legend indicates the values of $\Omega_1/(2\pi)$. The vertical-dotted line indicates $\chi/(2\pi) = 1$ MHz [$g_r/(2\pi) = 109.544$ MHz] used in (a) and (b), and also all the other figures of this article. This value satisfies the condition $\chi = \kappa/2$.

initial qubit states, $|0\rangle$ and $|1\rangle$, is the same since the state $|1\rangle$ eventually decays into the state $|0\rangle$. Therefore, we evolve the master equation for a finite time, which is long enough for the transients to disappear, but short enough that the state $|1\rangle$ does not decay significantly. We choose the evolution time $t_f = 20/\kappa \approx 1.6 \mu\text{s}$ in Fig. 5.

In Fig. 5(a), the arguments of the complex reflection coefficients $\arg(r)$ are shown as a function of probe frequency. For the probe frequency in the middle, $(\omega_d - \omega_r)/(2\pi) = 5$ MHz, close to the desired angle of π between the states $|0\rangle$ and $|1\rangle$ is obtained. To quantify how close the angle is to π , we calculate the smallest angle θ_d between the two complex

reflection coefficients via the dot product,

$$\cos \theta_d = \frac{\text{Re}[r_{|0\rangle}] \text{Re}[r_{|1\rangle}] + \text{Im}[r_{|0\rangle}] \text{Im}[r_{|1\rangle}]}{|r_{|0\rangle}| |r_{|1\rangle}|}, \quad (27)$$

where $r_{|0\rangle}$ and $r_{|1\rangle}$ are the reflection coefficients for the initial states $|0\rangle$ and $|1\rangle$, respectively. In Fig. 5(b), θ_d is shown as a function of the probe Rabi frequency Ω_1 .

Due to the transmon and resonator subsystem becoming more nonlinear for larger probe Rabi frequencies, the angle θ_d decreases. Addition of the JQF also decreases θ_d , although by a small fixed amount, about 1.5%. Despite choosing the parameters such that $\chi = \kappa/2$, the angle θ_d does not reach π even for a weak probe and without a JQF. This could be caused by the fact that the Schrieffer-Wolff transformation used to obtain the expression (19) for χ is a perturbative method and hence inexact. Other reasons for the discrepancy could be that our model does not make the dispersive approximation, under which the condition $\chi = \kappa/2$ is derived, and because there is some uncertainty with the heuristic procedure of choosing the finite evolution time t_f . We have verified that increasing χ (by increasing the coupling g_r) slightly is sufficient to reach the maximum angle of π , as shown in Fig. 5(c). In this subfigure, the angle θ_d is plotted as a function of the coupling χ for an optimal ω_d (obtained by the numerical optimization [39,40]). Once χ is large enough to obtain $\theta_d = \pi$ for a chosen probe power, the measurement is not expected to improve, but a larger coupling might still be useful for decreasing the gate time.

The above results suggest that the JQFs have a very similar behavior to the unsaturable band-rejection Purcell filters [9], in that each Purcell filter acts as a far off-resonant scatterer during the measurement, adding a small phase shift to the reflected field. Hence, if JQFs are combined with the frequency multiplexing, we expect the angle decrease between the computational basis states for each qubit to be small, as long as the number of the qubits in each multiplexed group is not much bigger than currently used (around 6 [1]). Other considerations for the frequency multiplexing that are not included in our model, such as the performance of the quantum limited amplifiers [41], are expected to play a much bigger role than the presence of the JQFs.

V. CONTROL

To verify the controllability of the system despite the complications arising from coupling to the qubit through the JQF and the resonator, we show that the Pauli σ_x gate can be implemented with high fidelity. For a two-level atom with a directly attached control line, this can be accomplished with a simple rectangular pulse. The setup where the two-level atom is replaced with a transmon and JQF added in the control line [Fig. 1(c)] requires pulses that are more carefully chosen [14,42]. For the setup that we are considering here [Fig. 1(d)], we use both the relatively simple pulses similar to Refs. [14,42,43] that do not require extensive calibration, and the more general Fourier series pulses inspired by Refs. [44,45] that achieve a larger gate fidelity.

We maximize the average gate fidelity. For a qubit, it is sufficient to average over the initial states at 6 cardinal points of the Bloch sphere, i.e., the eigenstates of the three Pauli

matrices [46]. More efficiently, the averaging could be done by propagating the Pauli matrices themselves with the master equation, even though these matrices are not valid states [46]. The system under consideration has more than two levels, but the states before and after a gate are mostly restricted to the qubit subspace. The leakage outside of the qubit subspace is accounted for by adding the states of the coupled transmon and resonator subsystem that also include the second excited state of the transmon and four excitations of the combined system in total. There are 12 such states. Together with 11 states of the JQF, this sets the total Hilbert space basis size of 132. In principle, more general expressions for the average fidelity need to be used with a much larger set of operators being propagated by the master equation [47]. To keep the simulation run time manageable, we use the expressions in Ref. [46] instead.

The expression for the average fidelity for the ideal operator $U = \sigma_x$ and the real superoperator \mathcal{M} that we use is thus

$$\tilde{F}_{\text{average}} = \frac{1}{4}\tilde{F}(I) + \frac{1}{12} \sum_{j=x,y,z} \tilde{F}(\sigma_j), \quad (28)$$

where

$$\tilde{F}(A) = \text{tr}_s[UAU^\dagger \mathcal{M}(A)]. \quad (29)$$

The Pauli matrices σ_j and the identity operator I in Eq. (28) are interpreted as operators on the entire (132-dimensional) Hilbert space but only have nonzero matrix elements for the qubit subspace. In Eq. (29), $\mathcal{M}(A)$ is calculated by initializing the master equation with the operator A instead of the initial density matrix and propagating until the final time t_f . It is not possible to simplify $\tilde{F}(I)$ to a constant like in Ref. [46], since I is not an identity operator on the entire Hilbert space. Compared to the fidelity F given by Eq. (24), the trace over the JQF is not performed in Eq. (29), requiring the JQF to be in the ground state $|0_2\rangle$ at the end of the gate. This ensures that the JQF does not disturb the qubit by emitting a photon after the gate is performed.

For the simpler pulse shape, we choose a Gaussian-filtered rectangular pulse

$$\text{Re}[\Omega](t) = \frac{\Omega_{\text{max}}}{\sigma_f \sqrt{2\pi}} \int_{t_{\text{start}}}^{t_{\text{end}}} \exp\left(-\frac{(t-t')^2}{2\sigma_f^2}\right) dt', \quad (30)$$

where $0 \leq t_{\text{start}}, t_{\text{end}} \leq t_f$. The above integral can be evaluated in terms of the error functions. The initial value $\text{Re}[\Omega](0)$ is never exactly zero, but t_{start} can be chosen such that $\text{Re}[\Omega](0)$ is below a certain tolerance $[\text{Re}[\Omega](0)/(2\pi)] < 0.2$ MHz in Fig. 6(c)]. The carrier frequency of the drive is set equal to the qubit transition frequency, i.e., $\omega_d = \omega_{1,10}$. Optionally, a correction is applied to the imaginary quadrature $\text{Im}[\Omega](t) = C_{\text{DRAG,Im}} \frac{d}{dt} \text{Re}[\Omega](t)$, and a power dependent frequency shift $\Delta_d(t) = C_{\text{DRAG,\Delta}} \text{Re}[\Omega]^2(t)$ is used similar to the Derivative Removal by Adiabatic Gate (DRAG) [43].

For a transmon without a JQF, the DRAG correction constants $C_{\text{DRAG,Im}}$ and $C_{\text{DRAG,\Delta}}$ have analytical expressions [43]. For our setup with the JQF, we find that these constants need

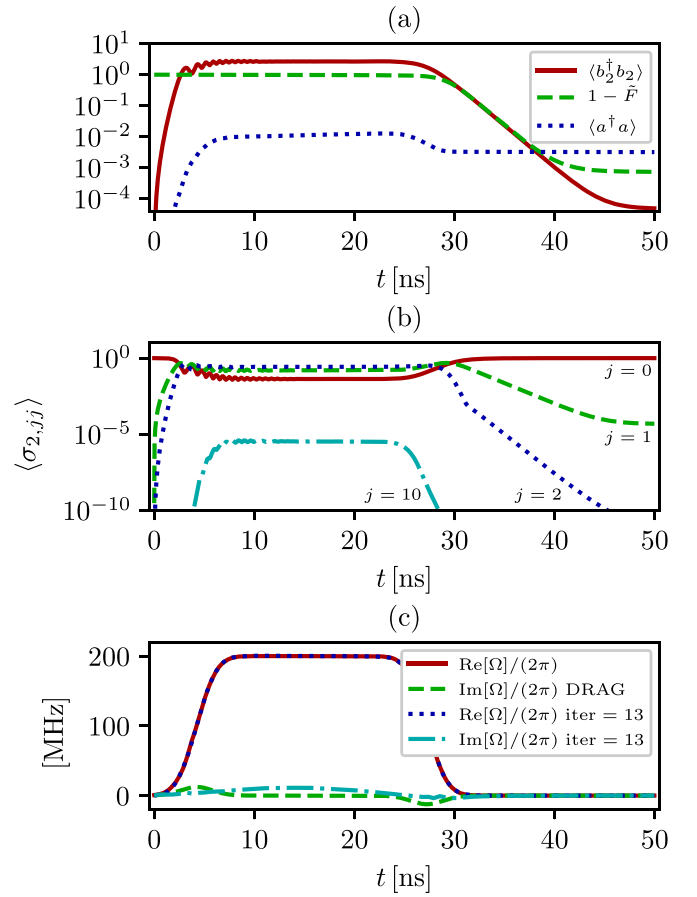


FIG. 6. The result of the simpler pulse shape [cf. Eq. (30)] optimization with a DRAG [43] correction. (a) The error probability $1 - \tilde{F}(|0\rangle\langle 0|)$ where $\tilde{F}(A)$ is given by Eq. (29), the resonator population $\langle a^\dagger a \rangle$, and the JQF population $\langle b_2^\dagger b_2 \rangle$ as functions of time for the setup initialized in the state $|0\rangle$ and driven to the state $\sigma_x|0\rangle = |1\rangle$ by the time-dependent Rabi frequency shown in (c) by the solid-red $[\text{Re}[\Omega](t)]$ and dashed-green $[\text{Im}[\Omega](t)]$ curves. In Eq. (30), we set $\Omega_{\text{max}}/(2\pi) = 200$ MHz, corresponding to -91 dBm [cf. Eq. (12)], and $1/\sigma_f = \kappa/0.02 = 628$ MHz. The DRAG corrections have the form: $\text{Im}[\Omega](t) = C_{\text{DRAG,Im}} \frac{d}{dt} \text{Re}[\Omega](t)$, and $\Delta_d(t) = C_{\text{DRAG,\Delta}} \text{Re}[\Omega]^2(t)$ (not shown) with $C_{\text{DRAG,Im}}$ and $C_{\text{DRAG,\Delta}}$ optimized numerically [39,40]. (b) Populations of the individual JQF levels $\langle \sigma_{2,jj} \rangle$. The achieved fidelity is $\tilde{F}(|0\rangle\langle 0|) = 0.9993$ ($\tilde{F}_{\text{average}} = 0.9981$). The dotted-blue $[\text{Re}[\Omega](t)]$ and dash-dotted-cyan $[\text{Im}[\Omega](t)]$ curves in (c) show the pulse shapes obtained after 13 iterations of the optimal control algorithm described in the text, using the initial pulse shape with $\text{Re}[\Omega](t)$ given by the solid-red curve and $\text{Im}[\Omega](t) = 0$. The achieved fidelity after 13 iterations is $\tilde{F}(|0\rangle\langle 0|) = 0.9993$ ($\tilde{F}_{\text{average}} = 0.9994$).

to be optimized numerically [39,40] to yield any improvement for the fidelity. However, the improvement is so small as to be negligible. Without the DRAG correction ($C_{\text{DRAG,Im}} = 0$ and $C_{\text{DRAG,\Delta}} = 0$), we get $\tilde{F}_{\text{average}} = 0.9980$. With the DRAG correction, $\tilde{F}_{\text{average}} = 0.9981$. Some of the initial states achieve higher fidelities, as shown in Fig. 6 with $\tilde{F}(|0\rangle\langle 0|) = 0.9993$. Using the optimal control approach described below with only 13 iterations, we see that a better correction $\text{Im}[\Omega](t)$ [the dash-dotted-cyan curve in Fig. 6(c)] is not proportional to the time derivative of $\text{Re}[\Omega](t)$, contrary to DRAG.

The optimal control with 13 iterations achieves $\tilde{F}_{\text{average}} = 0.9994$ ($\tilde{F}(|0\rangle\langle 0|) = 0.9993$) while keeping the pulse shapes simple.

To reach higher fidelities, we run the optimal control for more iterations. We consider the Fourier series parametrization of the pulses with a finite number of terms to limit the bandwidth. We can write this parametrization

$$\text{Re}[\Omega](t) = \sqrt{\frac{2}{t_f}} \sum_{p=1}^{N_c} a_p \sin(\omega_p t), \quad (31a)$$

$$\text{Im}[\Omega](t) = \sqrt{\frac{2}{t_f}} \sum_{p=1}^{N_c} b_p \sin(\omega_p t), \quad (31b)$$

where N_c is the maximum number of the Fourier components, and $\omega_p = p\pi/t_f$. By construction, $\sin(0) = \sin(\omega_p t_f) = 0$.

Optimizing a function with many variables (we choose $2N_c = 200$) is faster if a gradient-based algorithm is used. We use the reverse mode automatic differentiation, as explained in Appendix E, to calculate the gradient, which is used in the LBFGS algorithm [40,48] to find the maximum of $\tilde{F}_{\text{average}}$. For the reverse mode automatic differentiation, the cost of calculating the gradient is independent of the number of the variables $2N_c$. Using the fourth-order Runge-Kutta method for the propagation of the master equation, the time to calculate the fidelity and the gradient is around 8 times larger than the time to calculate the fidelity without the gradient.

For the initial qubit state $|0\rangle$, the resulting evolutions of the error probability $1 - \tilde{F}(|0\rangle\langle 0|)$ and the populations of the resonator and the JQF are shown in Fig. 7(a). The corresponding time-dependent Rabi frequency is shown in Fig. 7(c). The optimization has not finished after 2000 iterations taking around 50 days with the convergence rate becoming extremely small. It was run on a machine with a Ryzen 3700X CPU and a Radeon VII GPU, with the most computationally expensive part, the sparse matrix-vector multiplications, being performed on the GPU. A pure CPU calculation is about 4.5 times slower. Both implementations could be optimized further to speed up the calculations, and there may be a more efficient parametrization of the pulse shapes. Contrary to the setups without the JQF, we cannot perform the evolution in a closed system (with a Schrödinger equation) while optimizing the control pulse shapes [43], with the master equation only being used to evaluate the final pulses. The JQF has a short life time of $1/\gamma_2 = 1.6$ ns by design, which is much smaller than the gate time. Hence, a slower master equation evolution is needed to accurately simulate the dynamics also during the optimization.

The populations of the individual levels of the JQF are shown in Figs. 6(b) and 7(b). In both cases, the JQF is driven to the higher excitation levels by the strong control fields, effectively decoupling it from the transmission line and permitting control of the qubit. While the simpler pulses just reach some steady state level of the JQF population, the pulses found by optimal control induce fast oscillations, which result in a higher gate fidelity $\tilde{F}_{\text{average}} = 0.9996$ ($\tilde{F}(|0\rangle\langle 0|) = 0.9995$). For the optimal control parametrization (31), we use $N_c = 100$, giving the highest Fourier frequency $\omega_{N_c}/(2\pi) = 1$ GHz. Since it is possible to synthesize microwave pulses

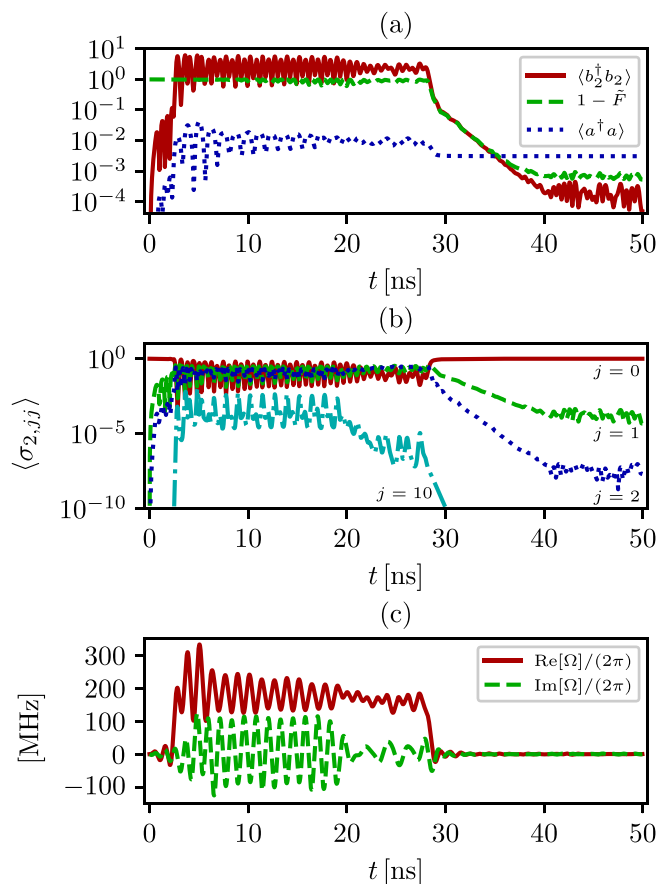


FIG. 7. The result of the optimal control. (a) The error probability $1 - \tilde{F}(|0\rangle\langle 0|)$ where $\tilde{F}(A)$ is given by Eq. (29), the resonator population $\langle a^\dagger a \rangle$, and the JQF population $\langle b_2^\dagger b_2 \rangle$ as functions of time for the setup initialized in the state $|0\rangle$ and driven to the state $\sigma_x|0\rangle = |1\rangle$ by the time-dependent Rabi frequency shown in (c). (b) Populations of the individual JQF levels $\langle \sigma_{2,jj} \rangle$. The achieved fidelity is $\tilde{F}(|0\rangle\langle 0|) = 0.9995$ ($\tilde{F}_{\text{average}} = 0.9996$). The number of the Fourier components in the parametrization (31) is $N_c = 100$ (for each of $\text{Re}[\Omega]$ and $\text{Im}[\Omega]$). This corresponds to the highest Fourier frequency $\omega_{N_c}/(2\pi) = 1$ GHz.

with bandwidths of several GHz [34,35,49], the pulse shapes in Fig. 7(c) are feasible.

Combination of the JQFs with the frequency multiplexing where multiple qubits are controlled by the same transmission line will likely require tuning of the control pulse shapes to reach high gate fidelities, because several qubit transitions will be within the bandwidth of the pulses shown in Figs. 6(c) and 7(c). Ideally, this would be accomplished by repeating the pulse shape optimizations using a Hilbert space that includes the entire system of several transmons and resonators. If the Hilbert space dimension 132 is used for each set of two transmons and a resonator that stores an filters one qubit (like we do for the simulations in this section), then the total Hilbert space dimension is 132^{N_q} with, e.g., $N_q = 6$ [1]. This makes the storage requirements for the density matrix prohibitive. It may be possible to side step this problem by using optimal control with the stochastic wave functions [50] or tensor networks [44]. Using the experimental setup directly is also an option [51].

VI. CONCLUSIONS

We have shown theoretically that it is possible to construct a saturable Purcell filter using an artificial atom directly attached to the transmission line. This filter suppresses the Purcell decay when the control fields are absent and can be effectively switched off by saturation when the control fields are present. This allows both the control and measurement of the qubit to be performed using a single transmission line while maintaining long coherence time. Our results can be used to decrease the number of the needed transmission lines in the superconducting quantum processors and other setups involving superconducting artificial atoms. Further reductions in the number of the transmission lines could be achieved by combining saturable Purcell filters with the frequency multiplexing.

ACKNOWLEDGMENTS

The authors acknowledge T. Shitara, S. Goto, and Y. Sunada for fruitful discussions. This work was supported by JST ERATO (Grant No. JPMJER1601), JST Moonshot R&D (Grants No. JPMJMS2067-3 and No. JPMJMS2061-2-1-2), and JSPS KAKENHI (Grant No. 22K03494).

APPENDIX A: DERIVATION OF THE MASTER EQUATION

In this Appendix, we derive the master equation (17), following Refs. [13,14,24,25]. The derivation is for N attached subsystems, i.e., not limited to $N = 2$ as in the main text. In this case, the summation in Hamiltonian given by Eq. (4) and the following ones is to N instead of 2; and Eqs. (5), (6), and (7) need to be redefined depending on the attached subsystems. Then the Heisenberg equations of motion for the field operators are

$$\dot{c}_\omega = -i\omega c_\omega - i \sum_{m=1}^N g_m(\omega)(\mathcal{O}_m - \mathcal{O}_m^\dagger) \quad (\text{A1})$$

with the solutions

$$c_\omega = c_\omega(0)e^{-i\omega t} - i \sum_{m=1}^N g_m(\omega) \times \int_0^t (\mathcal{O}_m(t-t') - \mathcal{O}_m^\dagger(t-t'))e^{-i\omega t'} dt'. \quad (\text{A2})$$

Here and below, the indication of the time-dependence of the operators is omitted for brevity as long as it is of the simple form: c_ω means $c_\omega(t)$ in the above expressions. Note that the term involving \mathcal{O}_m^\dagger is present, because the rotating wave approximation is not performed [24] in the Hamiltonian (4). Once we calculate

$$c_\omega - c_\omega^\dagger = c_\omega(0)e^{-i\omega t} - c_\omega^\dagger(0)e^{i\omega t} - i \sum_{m=1}^N g_m(\omega) \times \left(\int_0^t \mathcal{O}_m(t-t')(e^{-i\omega t'} - e^{i\omega t'}) dt' - \int_0^t \mathcal{O}_m^\dagger(t-t')(e^{-i\omega t'} - e^{i\omega t'}) dt' \right), \quad (\text{A3})$$

we see that terms arising from not performing the rotating wave approximation appear as additional $e^{\pm i\omega t'}$ in the inner parentheses. These will allow us to extend the integrations over ω to the entire real line.

The expression for $c_\omega - c_\omega^\dagger$ is needed in the Heisenberg equation of motion for an arbitrary system operator Q ,

$$\dot{Q} = \frac{i}{\hbar}[H_s, Q] + i \sum_{m=1}^N \int_0^\infty g_m(\omega) \times ([\mathcal{O}_m^\dagger, Q](c_\omega - c_\omega^\dagger) - (c_\omega - c_\omega^\dagger)[\mathcal{O}_m, Q])d\omega, \quad (\text{A4})$$

written in the normal ordered form. When we insert Eq. (A3), the normal ordering becomes important. The integrations over ω are carried out first. Using the expression for the coupling $g_m(\omega) = G_m\sqrt{\omega} \cos(k_\omega x_m)$, we have

$$\int_0^\infty g_m(\omega)g_n(\omega)(e^{-i\omega t'} - e^{i\omega t'})d\omega = \frac{i\pi G_m G_n}{2} \left(\dot{\delta}\left(t' - \frac{x_m - x_n}{v_g}\right) + \dot{\delta}\left(t' + \frac{x_m - x_n}{v_g}\right) + \dot{\delta}\left(t' - \frac{x_m + x_n}{v_g}\right) + \dot{\delta}\left(t' + \frac{x_m + x_n}{v_g}\right) \right), \quad (\text{A5})$$

where $\dot{\delta}$ is the derivative of the Dirac delta function that has the property

$$\int_0^t \dot{\delta}(t' - t_x)f(t-t')dt' = \dot{f}(t - t_x), \quad (\text{A6})$$

as long as $0 < t_x < t$, f is an arbitrary (operator-valued) function, and the integration limits are chosen as to be relevant to the present derivation. The case with $t_x = 0$ is defined with $\dot{f}(t)/2$ on the right hand side of Eq. (A6). Since $t_x = 0$ is equivalent to $x_m, x_n = 0$ in Eq. (A5), this case could also be addressed by setting $x_m, x_n = 0$ in the integral on the left hand side of Eq. (A5). Thus,

$$\int_0^t \left(\dot{\delta}\left(t' - \frac{x_m \pm x_n}{v_g}\right) + \dot{\delta}\left(t' + \frac{x_m \pm x_n}{v_g}\right) \right) \times \mathcal{O}_n(t-t')dt' = \dot{\mathcal{O}}_n\left(t - \frac{|x_m \pm x_n|}{v_g}\right)\theta_H\left(t - \frac{|x_m \pm x_n|}{v_g}\right), \quad (\text{A7})$$

where θ_H is the Heaviside theta function.

The integral in Eq. (A5) can also be evaluated with $g_m(\omega) = G_m(\sqrt{\omega}/\sqrt{1 + \mathcal{A}\omega^2}) \cos(k_\omega x_m)$ for $\mathcal{A} > 0$, resulting in

$$G_m G_n \int_0^\infty \frac{\omega \cos(k_\omega x_m) \cos(k_\omega x_n)}{1 + \mathcal{A}\omega^2} (e^{-i\omega t'} - e^{i\omega t'})d\omega = \left(\mathcal{K}\left(t' - \frac{x_m - x_n}{v_g}\right) + \mathcal{K}\left(t' + \frac{x_m - x_n}{v_g}\right) + \mathcal{K}\left(t' - \frac{x_m + x_n}{v_g}\right) + \mathcal{K}\left(t' + \frac{x_m + x_n}{v_g}\right) \right), \quad (\text{A8})$$

with

$$\mathcal{K}(t) = -\frac{i\pi G_m G_n}{4\mathcal{A}} \text{sgn}(t)e^{-|t|/\sqrt{\mathcal{A}}}, \quad (\text{A9})$$

and sgn being the sign function, $\text{sgn}(t) = 2\theta_H(t) - 1$. In this case, the time integral corresponding to Eq. (A7) cannot be evaluated explicitly. Since it is in a form of a convolution, the Laplace transform could be used [26], but there is no algorithm for the numerical inverse Laplace transform that can work in all cases, necessitating selection among the different available algorithms [52–54]. For simplicity, we find the Markovian master equation using a different integration order (first t then ω instead of first ω then t) and using the approximation (9) or (10) from the beginning, as detailed in Appendix B.

For the rest of this Appendix, we continue with the coupling $g_m(\omega) = G_m\sqrt{\omega} \cos(k_\omega x_m)$. Defining the noise operator

$$\mathcal{N}_m = \int_0^\infty g_m(\omega) c_\omega(0) e^{-i\omega t} d\omega, \quad (\text{A10})$$

and applying the rotating wave approximation, we can write

$$\begin{aligned} \dot{Q} = & \frac{i}{\hbar} [H_s, Q] + i \sum_{m=1}^N ([\mathcal{O}_m^\dagger, Q] \mathcal{N}_m + \mathcal{N}_m^\dagger [\mathcal{O}_m, Q]) \\ & + \sum_{m,n=1}^N \frac{i\pi G_m G_n}{2} [\mathcal{O}_m^\dagger, Q] \left(\dot{\mathcal{O}}_n \left(t - \frac{|x_m - x_n|}{v_g} \right) \right. \\ & \left. + \dot{\mathcal{O}}_n \left(t - \frac{|x_m + x_n|}{v_g} \right) \right) \\ & + \sum_{m,n=1}^N \frac{i\pi G_m G_n}{2} \left(\dot{\mathcal{O}}_n^\dagger \left(t - \frac{|x_m - x_n|}{v_g} \right) \right. \\ & \left. + \dot{\mathcal{O}}_n^\dagger \left(t - \frac{|x_m + x_n|}{v_g} \right) \right) [\mathcal{O}_m, Q], \quad (\text{A11}) \end{aligned}$$

where the Heaviside theta function factors resulting from Eq. (A7) are implicit. We make one more approximation by setting

$$\dot{\mathcal{O}}_n(t - t_x) \approx -i \sum_{j,j'} \omega_{n,j'j} C_{n,j'j} \sigma_{n,j'j}(t - t_x), \quad (\text{A12})$$

where $\omega_{n,j'j} = \omega_{n,j'} - \omega_{n,j}$. This approximation can be viewed as applying Eq. (A11) and ignoring all the terms besides $\frac{i}{\hbar} [H_s, \mathcal{O}_n]$ due to the fact that the absolute frequencies $\omega_{n,j'j}$ are large compared to the couplings G_n . Thus, this is also a form of a rotating wave approximation.

In Appendix C, the equations of motion in the single-excitation subspace are derived from Eq. (A11) without any further approximations besides Eq. (A12). For the master equation (17), Eq. (A11) needs to be approximated such that it becomes local in time, i.e., does not contain operators at the previous times $t - |x_m \pm x_n|/v_g$. We use either approximation (9) or (10) together with the approximation (A12). Additionally, we assume that the size of the ensemble is small, i.e., $|x_m \pm x_n|/v_g$ is short compared to the time scales of interest, and hence we set $\theta_H(t - |x_m \pm x_n|/v_g) = 1$ for all t .

Using the approximation (9), inserting $G_m = \sqrt{\Gamma_m/(2\pi\omega_m)}$, identifying $\xi_{mn,j'j}$ given by Eq. (18) and

$\mathcal{O}_{mn} = \sum_{j,j'} \xi_{mn,j'j} C_{n,j'j} \sigma_{n,j'j}$, we get

$$\begin{aligned} \dot{Q} = & \frac{i}{\hbar} [H_s, Q] + i \sum_{m=1}^N ([\mathcal{O}_m^\dagger, Q] \mathcal{N}_m + \mathcal{N}_m^\dagger [\mathcal{O}_m, Q]) \\ & + \frac{1}{2} \sum_{m,n=1}^N ([\mathcal{O}_m^\dagger, Q] \mathcal{O}_{mn} - \mathcal{O}_{mn}^\dagger [\mathcal{O}_m, Q]). \quad (\text{A13}) \end{aligned}$$

The above equation with the drive approximation (10) is obtained by setting $k_{n,j'j} = k_{\omega_d}$ in Eq. (18).

Since the expectation values are the same in the Heisenberg and Schrödinger pictures, we have

$$\langle Q \rangle = \text{tr}_s \text{tr}_f [Q \rho(0)] = \text{tr}_s [Q(0) \rho_s], \quad (\text{A14})$$

where tr_s (tr_f) is the trace over the system (field) degrees of freedom, and $\rho_s = \text{tr}_f[\rho]$. Taking the time derivative, we get

$$\text{tr}_s \text{tr}_f [\dot{Q} \rho(0)] = \text{tr}_s [Q(0) \dot{\rho}_s]. \quad (\text{A15})$$

The procedure to obtain the master equation (17) starts with inserting Eq. (A13) into the left-hand side of Eq. (A15). The resulting expression can then be rewritten in the form $\text{tr}_s [Q(0) B]$, where B is some system operator expression. Using the right-hand side of Eq. (A15), the master equation is obtained as $\dot{\rho}_s = B$.

For any system operator A ,

$$\text{tr}_s \text{tr}_f [[A, Q] \rho(0)] = -\text{tr}_s [Q(0) [A(0), \rho_s]]. \quad (\text{A16})$$

In $\text{tr}_s \text{tr}_f [[\mathcal{O}_m^\dagger, Q] \mathcal{N}_m \rho(0)]$ and $\text{tr}_s \text{tr}_f [\mathcal{N}_m^\dagger [\mathcal{O}_m, Q] \rho(0)]$, we assume that $\rho(0) = \rho_s(0) \otimes \rho_f(0)$ with the state of the field $\rho_f(0) = |\{\alpha_\omega\}\rangle \langle \{\alpha_\omega\}|$ being a multimode coherent state. This state could be written as the displaced vacuum state $|\{\alpha_\omega\}\rangle = D(\{\alpha_\omega\})|\text{vac}\rangle$, where the displacement operator is

$$D(\{\alpha_\omega\}) = \exp \left(\int_0^\infty (\alpha_\omega c_\omega^\dagger(0) - \alpha_\omega^* c_\omega(0)) d\omega \right). \quad (\text{A17})$$

We have

$$c_\omega(0) |\{\alpha_\omega\}\rangle = \alpha_\omega |\{\alpha_\omega\}\rangle. \quad (\text{A18})$$

To relate α_ω to the photon flux \dot{n} , we define Fourier transformed operators [55]

$$c_t = \frac{1}{\sqrt{2\pi}} \int_0^\infty c_\omega(0) e^{-i\omega t} d\omega, \quad (\text{A19})$$

and then the photon flux is $\dot{n} = \langle c_t^\dagger c_t \rangle = |\alpha_t|^2$, where

$$\alpha_t = \frac{1}{\sqrt{2\pi}} \int_0^\infty \alpha_\omega e^{-i\omega t} d\omega. \quad (\text{A20})$$

For the operators (A10), it holds that

$$\mathcal{N}_m |\{\alpha_\omega\}\rangle = \Omega_m e^{-i\omega_d t} |\{\alpha_\omega\}\rangle, \quad (\text{A21})$$

where we have defined the Rabi frequency

$$\Omega_m e^{-i\omega_d t} = \int_0^\infty g_m(\omega) \alpha_\omega e^{-i\omega t} d\omega. \quad (\text{A22})$$

To go from Eq. (A22) to Eq. (12), a narrow-bandwidth approximation is made, $g_m(\omega) \approx g_m(\omega_d)$, resulting in $\Omega_m e^{-i\omega_d t} = \sqrt{2\pi} g_m(\omega_d) \alpha_t$. Since $\dot{n} = |\alpha_t|^2$, we set $\alpha_t = \sqrt{\dot{n}} e^{-i\omega_d t} e^{i\phi}$ for some phase ϕ , and then Eq. (12) is obtained. For the reflection coefficient calculations (Sec. IV and Appendix D), we also

need to consider the case of the infinitely narrow bandwidth continuous wave input, where

$$c_\omega(0)|\{\alpha_\omega\}\rangle = \sqrt{2\pi\hbar}e^{i\phi}\delta(\omega - \omega_d)|\{\alpha_\omega\}\rangle. \quad (\text{A23})$$

Using Eq. (A21), the terms $\text{tr}_s \text{tr}_f[[\mathcal{O}_m^\dagger, \mathcal{Q}]\mathcal{N}_m\rho(0)]$ and $\text{tr}_s \text{tr}_f[\mathcal{N}_m^\dagger[\mathcal{O}_m, \mathcal{Q}]\rho(0)]$ are simplified into the form where Eq. (A16) can be applied. These terms give rise to the drive Hamiltonian (11). Together with the other terms rewritten either using either Eq. (A16) or in a similar way, we get the master equation

$$\begin{aligned} \dot{\rho}_s = & -\frac{i}{\hbar}[H_d + H_s, \rho_s] + \frac{1}{2} \sum_{m,n=1}^N (\mathcal{O}_{mn}\rho_s\mathcal{O}_m^\dagger - \mathcal{O}_m^\dagger\mathcal{O}_{mn}\rho_s) \\ & + \frac{1}{2} \sum_{m,n=1}^N (\mathcal{O}_n\rho_s\mathcal{O}_{nm}^\dagger - \rho_s\mathcal{O}_{nm}^\dagger\mathcal{O}_n). \end{aligned} \quad (\text{A24})$$

Transforming Eq. (A24) into the rotating frame with respect to the Hamiltonian (13) by substituting $\rho_s = e^{-iH_0t/\hbar}\tilde{\rho}_s e^{iH_0t/\hbar}$ results in the master equation (17) with

$$\dot{\tilde{H}} = e^{iH_0t/\hbar}(H_d + H_s)e^{-iH_0t/\hbar} - H_0. \quad (\text{A25})$$

Frequencies $\omega_{0,m,j}$ in Eq. (13) are chosen such that $\frac{i}{\hbar}[H_0, \mathcal{O}_m] = -i\omega_d\mathcal{O}_m$, and thus the factors $e^{\pm i\omega_d t}$ in Eq. (11) are canceled. By inserting $\mathcal{O}_m = C_{m,jj'}\sigma_{m,jj'}$, the equivalent condition is

$$\omega_{0,m,j'} - \omega_{0,m,j} = \omega_d \quad (\text{A26})$$

for every $C_{m,jj'} \neq 0$. It is possible to satisfy this condition, since \mathcal{O}_m is an annihilation operator, and hence $C_{m,jj'} \neq 0$ only if j and j' correspond to the eigenstates with excitation numbers $N_{m,j}$ and $N_{m,j'} = N_{m,j} + 1$, respectively. Thus, setting $\omega_{0,m,j} = N_{m,j}\omega_d$ satisfies Eq. (A26). With this choice, Eq. (A25) becomes Eq. (14).

APPENDIX B: CUTOFF IN THE COUPLING

In this Appendix, we derive the master equation using the coupling between the subsystems and the transmission line $g_m(\omega) = G_m(\sqrt{\omega}/\sqrt{1 + \mathcal{A}\omega^2})\cos(k_\omega x_m)$ with $\mathcal{A} > 0$ [20–23] instead of $g_m(\omega) = G_m\sqrt{\omega}\cos(k_\omega x_m)$ that was used in all of the main text and the other appendices. Similar to Appendix A, N attached subsystems are considered, instead of setting $N = 2$ as in the main text. The discussion of the challenges associated with not using any approximations can be found below Eq. (A8) in Appendix A. For simplicity, we use the approximation (9) from the beginning (using the approximation (10) is accomplished by replacing the frequencies). Inserting $\mathcal{O}_m = \sum_{j,j'} C_{m,jj'}\sigma_{m,jj'}$ into Eq. (A2), applying the approximation (9), and setting $\omega_{m,j'j} = \omega_{m,j'} - \omega_{m,j}$, gives

$$\begin{aligned} c_\omega = & c_\omega(0)e^{-i\omega t} \\ & - i \sum_{m=1}^N \sum_{j,j'} g_m(\omega) \int_0^t (C_{m,jj'}\sigma_{m,jj'} e^{-i(\omega - \omega_{m,j'j})t'}) \\ & - C_{m,jj'}^* \sigma_{m,jj'} e^{-i(\omega + \omega_{m,j'j})t'}) dt'. \end{aligned} \quad (\text{B1})$$

Following Ref. [25], the time integral could be approximated by extending the upper limit to infinity and using the identity

(related to the Sokhotski-Plemelj theorem)

$$\int_0^\infty e^{\pm i\epsilon s} ds = \pi\delta(\epsilon) \pm i\text{PV}\frac{1}{\epsilon}, \quad (\text{B2})$$

where PV means the principal value. Hence,

$$\begin{aligned} c_\omega = & c_\omega(0)e^{-i\omega t} - i \sum_{m=1}^N \sum_{j,j'} g_m(\omega) \\ & \times \left(C_{m,jj'}\sigma_{m,jj'} \left(\delta(\omega - \omega_{m,j'j}) - i\text{PV}\frac{1}{\omega - \omega_{m,j'j}} \right) \right. \\ & \left. - C_{m,jj'}^*\sigma_{m,jj'} \left(\delta(\omega + \omega_{m,j'j}) - i\text{PV}\frac{1}{\omega + \omega_{m,j'j}} \right) \right). \end{aligned} \quad (\text{B3})$$

When inserting the above into Eq. (A4), two different integrals over the frequency need to be performed,

$$\begin{aligned} \text{Re}[\xi_{mn,j'j}] = & 2\pi \int_0^\infty g_m(\omega)g_n(\omega) \\ & \times (\delta(\omega - \omega_{n,j'j}) - \delta(\omega + \omega_{n,j'j}))d\omega, \end{aligned} \quad (\text{B4a})$$

$$\text{Im}[\xi_{mn,j'j}] = -2\text{PV} \int_0^\infty g_m(\omega)g_n(\omega) \frac{2\omega}{\omega^2 - \omega_{n,j'j}^2} d\omega; \quad (\text{B4b})$$

and then the same Eq. (A13) is obtained with $\mathcal{O}_{mn} = \sum_{j,j'} \xi_{mn,j'j} C_{n,jj'}\sigma_{n,jj'}$, but $\xi_{mn,j'j}$ is given by the integrals (B4) instead of Eq. (18). The integrands of both of the integrals (B4) are different if the rotating wave approximation is performed already in the Hamiltonian (4), again illustrating the importance of delaying this approximation until after these integrals are evaluated [24].

To evaluate the integrals (B4), a particular form of the coupling $g_m(\omega)$ needs to be chosen. Using $g_m(\omega) = G_m(\sqrt{\omega}/\sqrt{1 + \mathcal{A}\omega^2})\cos(k_\omega x_m)$, we get the real part

$$\begin{aligned} \text{Re}[\xi_{mn,j'j}] = & \pi G_m G_n \frac{\omega_{n,j'j}}{1 + \mathcal{A}\omega_{n,j'j}^2} (\cos(k_{|\omega_{n,j'j}|}(x_m - x_n)) \\ & + \cos(k_{|\omega_{n,j'j}|}(x_m + x_n))). \end{aligned} \quad (\text{B5})$$

For the imaginary part, we first switch to the integration over $k = \omega/v_g$, so that we need to evaluate the integral of the form

$$I(x) = \text{PV} \int_0^\infty \frac{2k^2}{(1 + \mathcal{A}v_g^2 k^2)(k^2 - k_{n,j'j}^2)} \cos(kx) dk, \quad (\text{B6})$$

where $k_{n,j'j} = k_{\omega_{n,j'j}}$. Then

$$\text{Im}[\xi_{mn,j'j}] = -G_m G_n v_g (I(x_m - x_n) + I(x_m + x_n)). \quad (\text{B7})$$

The evaluation of the integral (B6) can be done by integrating in the complex plane and using the residue theorem. After further variable changes, the integral is written

$$I(x) = \frac{1}{|x|} \text{PV} \int_{-\infty}^\infty f_I(z) dz, \quad (\text{B8})$$

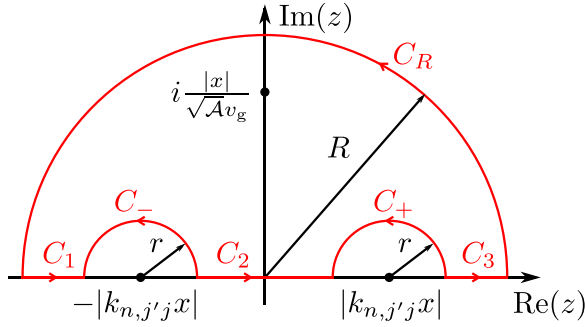


FIG. 8. The complex contour (red) used for evaluation of the integral (B8). The three relevant poles of the integrand (B9) at $-|k_{n,j}x|$, $|k_{n,j}x|$, and $i|x|/(\sqrt{A}v_g)$ are shown as dots. The half-circle C_R is parametrized by the radius $R \rightarrow \infty$. The half-circles C_{\pm} are parametrized by the radius $r \rightarrow 0$. The direction of integration along the sections is shown with arrows.

with the integrand

$$f_I(z) = \frac{2\left(\frac{z}{x}\right)^2}{\left(1 + \mathcal{A}v_g^2\left(\frac{z}{x}\right)^2\right)\left(\left(\frac{z}{x}\right)^2 - k_{n,j}^2\right)} e^{iz}. \quad (\text{B9})$$

The integral (B8) is then evaluated using the complex contour shown in Fig. 8. The principal value is found by using half-circles with a radius r around the poles of f_I lying on the real line and then letting $r \rightarrow 0$. A large half-circle with the radius $R \rightarrow \infty$ encloses the pole on the positive imaginary axis.

Defining

$$I_C = \lim_{R \rightarrow \infty, r \rightarrow 0} \frac{1}{|x|} \text{PV} \int_C f_I(z) dz \quad (\text{B10})$$

to be the integral along each section C of the contour, and $\text{Res}(f_I(z), c)$ to be the residue of the function f_I at $z = c$, we see that the integral to do is

$$I(x) = I_{C_1} + I_{C_2} + I_{C_3}, \quad (\text{B11})$$

while for the entire contour, it holds that

$$\begin{aligned} I_{C_1} - I_{C_-} + I_{C_2} - I_{C_+} + I_{C_3} + I_{C_R} \\ = \frac{2\pi i}{|x|} \text{Res}\left(f_I(z), i\frac{|x|}{\sqrt{A}v_g}\right), \end{aligned} \quad (\text{B12})$$

where the signs are determined according to the directions shown by the arrows in Fig. 8.

For large $|z|$, it holds that $|f_I(x)| \leq M/|z|^2$ with $M = 2x^2/(\mathcal{A}v_g^2)$. This is a sufficient condition to show that $I_{C_R} = 0$. Therefore, we have

$$I(x) = \frac{2\pi i}{|x|} \text{Res}\left(f_I(z), i\frac{|x|}{\sqrt{A}v_g}\right) + I_{C_+} + I_{C_-}, \quad (\text{B13})$$

where

$$I_{C_{\pm}} = \frac{\pi i}{|x|} \text{Res}(f_I(z), \pm|k_{n,j}x|). \quad (\text{B14})$$

For simple poles, like we have here, it holds that $\text{Res}(f_I(z), c) = \lim_{z \rightarrow c} (z - c)f_I(z)$. Hence,

$$I(x) = \frac{\pi}{1 + \mathcal{A}\omega_{n,j}^2} \left(\frac{e^{-|x|/(\sqrt{A}v_g)}}{\sqrt{A}v_g} - k_{n,j} \sin(k_{n,j}|x|) \right), \quad (\text{B15})$$

and

$$\begin{aligned} \xi_{mn,j} = \frac{\pi G_m G_n}{1 + \mathcal{A}\omega_{n,j}^2} \\ \times \left(-\frac{ie^{-|x_m - x_n|/(\sqrt{A}v_g)}}{\sqrt{A}} + \omega_{n,j} e^{ik_{n,j}|x_m - x_n|} \right. \\ \left. - \frac{ie^{-|x_m - x_n|/(\sqrt{A}v_g)}}{\sqrt{A}} + \omega_{n,j} e^{ik_{n,j}|x_m + x_n|} \right). \end{aligned} \quad (\text{B16})$$

Therefore, for $g_m(\omega) = G_m(\sqrt{\omega}/\sqrt{1 + \mathcal{A}\omega^2}) \cos(k_{\omega}x_m)$ with $\mathcal{A} > 0$ and following the same steps as in Appendix A after Eq. (A13), we see that the factor $\xi_{mn,j}$ in the master equation (17) is given by Eq. (B16) instead of Eq. (18). For $A \rightarrow 0^+$ and $G_m = \sqrt{\Gamma_m/(2\pi\omega_m)}$, Eq. (B16) becomes Eq. (18), as expected.

APPENDIX C: DELAY DIFFERENTIAL EQUATIONS FOR THE DECAY

In this Appendix, we derive the model for the decay without the approximations (9) or (10), following the approach of Ref. [13]. In the single-excitation subspace, only 3 subsystem states are relevant: a single excitation in either of the transmons or the resonator. Using the diagonal basis, the subsystem 1 consisting of the transmon and the resonator is represented by the two eigenstates (21) with the eigenfrequencies (22). For the subsystem 2 (JQF), there is only one eigenstate $|1_2\rangle$ to consider. In the single-excitation subspace, we therefore have

$$\mathcal{O}_1 = a = C_{1,01}\sigma_{1,01} + C_{1,02}\sigma_{1,02}, \quad (\text{C1a})$$

$$\mathcal{O}_2 = b_2 = C_{2,01}\sigma_{2,01}, \quad (\text{C1b})$$

where $C_{1,01} = \langle 0_1|a|1_1\rangle = \sin(\theta)$, $C_{1,02} = \langle 0_1|a|2_1\rangle = \cos(\theta)$, and $C_{2,01} = \langle 0_2|b_2|1_2\rangle = 1$.

Equations of motion for the operators $\sigma_{m,0j}$ are obtained from Eq. (A11) under the approximation (A12). We consider the single-excitation state

$$\begin{aligned} |\psi(t)\rangle = \sum_{m,j} \alpha_{m,j}(t) \sigma_{m,j0}(0) |\text{vac}\rangle \\ + \int_0^\infty f_\omega(t) c_\omega^\dagger(0) d\omega |\text{vac}\rangle, \end{aligned} \quad (\text{C2})$$

where $|\text{vac}\rangle = |0_1\rangle|0_2\rangle|\text{vac}_c\rangle$, and $|\text{vac}_c\rangle$ is the vacuum state for the transmission line. The equations of motion for the amplitudes $\alpha_{m,j}$ are found as

$$\dot{\alpha}_{m,j}(t) = \langle \text{vac} | \dot{\sigma}_{m,0j}(t) | \psi(0) \rangle. \quad (\text{C3})$$

Defining the inputs $f_{in,m}(t) = \int_0^\infty g_m(\omega) f_\omega(0) e^{-i\omega t} d\omega$, slowly-varying quantities $\alpha_{m,j}(t) = \tilde{\alpha}_{m,j}(t) e^{-i\omega_{1,10} t}$ and $\tilde{f}_{in,m}(t) = \tilde{f}_{in,m}(t) e^{-i\omega_{1,10} t}$, and setting $x_1 = 0$ for simplicity, gives the delay differential equations

$$\dot{\tilde{\alpha}}_{1,1}(t) = -iC_{1,01}^* \tilde{f}_{in,1}(t) - |C_{1,01}|^2 \frac{\kappa}{2} \frac{\omega_{1,10}}{\omega_r} \tilde{\alpha}_{1,1}(t) - C_{1,01}^* C_{1,02} \frac{\kappa}{2} \frac{\omega_{1,20}}{\omega_r} \tilde{\alpha}_{1,2}(t) \quad (C4a)$$

$$- C_{1,01}^* C_{2,01} \frac{\sqrt{\kappa\gamma_2}}{2} \frac{\omega_{2,10}}{\sqrt{\omega_r\omega_{t,2}}} e^{ik_{\omega_{1,10}}x_2} \tilde{\alpha}_{2,1}(t - x_2/v_g), \quad (C4b)$$

$$\dot{\tilde{\alpha}}_{1,2}(t) = -i(\omega_{1,20} - \omega_{1,10}) \tilde{\alpha}_{1,2}(t) - iC_{1,02}^* \tilde{f}_{in,1}(t) - |C_{1,02}|^2 \frac{\kappa}{2} \frac{\omega_{1,20}}{\omega_r} \tilde{\alpha}_{1,2}(t) - C_{1,02}^* C_{1,01} \frac{\kappa}{2} \frac{\omega_{1,10}}{\omega_r} \tilde{\alpha}_{1,1}(t)$$

$$- C_{1,02}^* C_{2,01} \frac{\sqrt{\kappa\gamma_2}}{2} \frac{\omega_{2,10}}{\sqrt{\omega_r\omega_{t,2}}} e^{ik_{\omega_{1,10}}x_2} \tilde{\alpha}_{2,1}(t - x_2/v_g),$$

$$\dot{\tilde{\alpha}}_{2,1}(t) = -i(\omega_{2,10} - \omega_{1,10}) \tilde{\alpha}_{2,1}(t) - iC_{2,01}^* \tilde{f}_{in,2}(t) - |C_{2,01}|^2 \frac{\gamma_2}{4} \frac{\omega_{2,10}}{\omega_{t,2}} (\tilde{\alpha}_{2,1}(t) + e^{2ik_{\omega_{1,10}}x_2} \tilde{\alpha}_{2,1}(t - 2x_2/v_g))$$

$$- C_{2,01}^* C_{1,01} \frac{\sqrt{\kappa\gamma_2}}{2} \frac{\omega_{1,10}}{\sqrt{\omega_r\omega_{t,2}}} e^{ik_{\omega_{1,10}}x_2} \tilde{\alpha}_{1,1}(t - x_2/v_g) - C_{2,01}^* C_{1,02} \frac{\sqrt{\kappa\gamma_2}}{2} \frac{\omega_{2,10}}{\sqrt{\omega_r\omega_{t,2}}} e^{ik_{\omega_{1,10}}x_2} \tilde{\alpha}_{1,2}(t - x_2/v_g), \quad (C4c)$$

where the appropriate Heaviside theta function factors on the delayed terms are implicit.

We set the initial conditions $\tilde{\alpha}_{1,1}(0) = 1$, $\tilde{\alpha}_{1,2}(0) = \tilde{\alpha}_{2,1}(0) = 0$, $f_\omega(0) = 0$, and use the Euler method for the numerical solution. The Runge-Kutta method applied to the delay differential equations requires accurate interpolations between the time steps [56]. For the Euler method, if the delays x_2/v_g are an integer multiple of the step size, no such interpolation is required. The drawback is a significantly larger number of time steps N_t required to reach convergence. We use $N_t = 4 \times 10^{12}$ in Fig. 9(b). Compared to the

master equation curves in Fig. 9(a), the ‘‘steady-state’’ value in Fig. 9(b) is shifted by about 5×10^{-7} .

APPENDIX D: DERIVATION OF THE REFLECTION COEFFICIENT

In this Appendix, we derive the input-output relations corresponding to the master equation (17). As in Appendix A, the general setup with N attached subsystems is considered, generalizing from the case $N = 2$ in the main text. The voltage operator in the transmission line is

$$V(x) = -i\sqrt{\frac{\hbar Z_0}{\pi}} \int_0^\infty \sqrt{\omega} (c_\omega - c_\omega^\dagger) \cos(k_\omega x) d\omega, \quad (D1)$$

where Z_0 is the impedance of the transmission line. With the charge number operators $n_m \propto -i(\mathcal{O}_m - \mathcal{O}_m^\dagger)$ for the subsystems attached to the transmission line, the above expression for $V(x)$ determines the interaction Hamiltonian $H_i \propto \sum_{m=1}^N V(x_m) n_m$, resulting in Eq. (4). This can be shown by performing the circuit quantization of the setup (ignoring the A^2 term).

The voltage operator is split into the right-moving (V_+) and left-moving (V_-) parts, $V(x) = V_+(x) + V_-(x)$, where

$$V_\pm(x) = -i\sqrt{\frac{\hbar Z_0}{4\pi}} \int_0^\infty \sqrt{\omega} (c_\omega e^{\pm ik_\omega x} - c_\omega^\dagger e^{\mp ik_\omega x}) d\omega. \quad (D2)$$

We have

$$\begin{aligned} & c_\omega e^{\pm ik_\omega x} - c_\omega^\dagger e^{\mp ik_\omega x} \\ &= c_\omega(0) e^{-i\omega t \pm ik_\omega x} - c_\omega^\dagger(0) e^{i\omega t \mp ik_\omega x} - i \sum_{m=1}^N g_m(\omega) \\ & \times \left(\int_0^t \mathcal{O}_m(t-t') (e^{-i\omega t' \pm ik_\omega x} - e^{i\omega t' \mp ik_\omega x}) dt' \right. \\ & \left. - \int_0^t \mathcal{O}_m^\dagger(t-t') (e^{-i\omega t' \pm ik_\omega x} - e^{i\omega t' \mp ik_\omega x}) dt' \right). \quad (D3) \end{aligned}$$

The same comment about Eq. (A3) applies to Eq. (D3)—that additional terms are present due to not making the rotating wave approximation in the Hamiltonian (4).

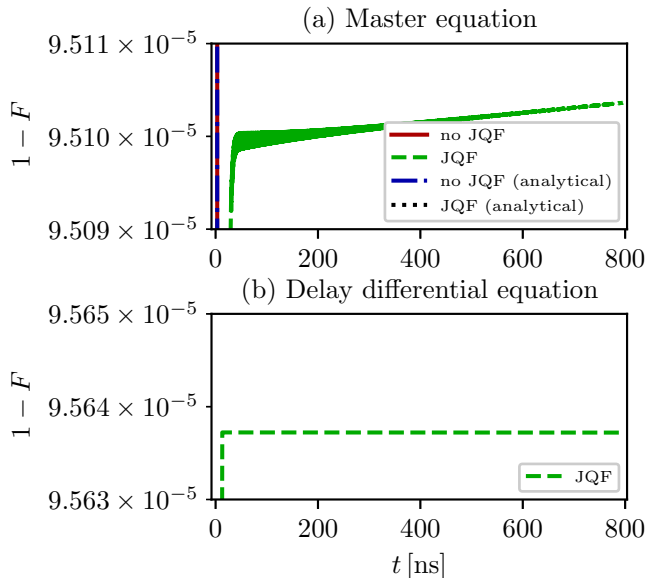


FIG. 9. (a) The zoomed-in version of Fig. 3, using the master equation (17) for the numerical results. Rapid oscillations of the dashed-green curve make it appear thick for smaller times. The horizontal-dotted-black line showing Eq. (25) is below the lower limit of the vertical axis by about 2×10^{-8} and hence cannot be seen. (b) The setup with a JQF corresponding to the dashed green curve of (a), but calculated using the delay differential equations (C4). In (b), $F = |\tilde{\alpha}_{1,1}(t)|^2$.

Only after calculating $c_\omega e^{\pm ik_\omega x} - c_\omega^\dagger e^{\mp ik_\omega x}$, the resulting expression can be split into two parts involving either creation or annihilation operators. That is, we write $V_\pm(x) = \mathcal{V}_\pm(x) + \mathcal{V}_\pm^\dagger(x)$, where

$$\begin{aligned} \mathcal{V}_\pm(x) &= \mathcal{V}_{\pm,0}(x) \\ &- \sqrt{\frac{\hbar Z_0}{4\pi}} \sum_{m=1}^N \int_0^t \mathcal{O}_m(t-t') \int_0^\infty \sqrt{\omega} g_m(\omega) \\ &\times (e^{-i\omega t' \pm ik_\omega x} - e^{i\omega t' \mp ik_\omega x}) d\omega dt', \end{aligned} \quad (\text{D4})$$

and

$$\mathcal{V}_{\pm,0}(x) = -i\sqrt{\frac{\hbar Z_0}{4\pi}} \int_0^\infty \sqrt{\omega} c_\omega(0) e^{-i\omega t \pm ik_\omega x} d\omega. \quad (\text{D5})$$

The integral over ω in Eq. (D4) is similar to the integral in Eq. (A5), and we get

$$\begin{aligned} &\int_0^\infty \sqrt{\omega} g_m(\omega) (e^{-i\omega t' \pm ik_\omega x} - e^{i\omega t' \mp ik_\omega x}) d\omega \\ &= i\pi G_m \left(\dot{\delta} \left(t' \mp \frac{x-x_m}{v_g} \right) + \dot{\delta} \left(t' \mp \frac{x+x_m}{v_g} \right) \right). \end{aligned} \quad (\text{D6})$$

While up to now the calculation for the right-moving and left-moving parts was symmetric, the asymmetry arises after the integration over t' . Using Eq. (A6),

$$\begin{aligned} \mathcal{V}_+(x) &= \mathcal{V}_{+,0}(x) - \sqrt{\frac{\hbar Z_0}{4\pi}} \sum_{m=1}^N (i\pi) G_m \\ &\times \left(\dot{\mathcal{O}}_m \left(t - \frac{x-x_m}{v_g} \right) \theta_H \left(t - \frac{x-x_m}{v_g} \right) \theta_H(x-x_m) \right. \\ &\left. + \dot{\mathcal{O}}_m \left(t - \frac{x+x_m}{v_g} \right) \theta_H \left(t - \frac{x+x_m}{v_g} \right) \right), \end{aligned} \quad (\text{D7a})$$

$$\begin{aligned} \mathcal{V}_-(x) &= \mathcal{V}_{-,0}(x) - \sqrt{\frac{\hbar Z_0}{4\pi}} \sum_{m=1}^N (i\pi) G_m \\ &\times \dot{\mathcal{O}}_m \left(t - \frac{x_m-x}{v_g} \right) \theta_H \left(t - \frac{x_m-x}{v_g} \right) \theta_H(x_m-x). \end{aligned} \quad (\text{D7b})$$

The right-moving part \mathcal{V}_+ has two types of contributions: those that are emitted directly to the right and those that are emitted to the left and then reflected from the boundary at $x=0$. The left-moving part \mathcal{V}_- only has contributions from the emission directly to the left.

Under the approximations (A12) and (10),

$$\begin{aligned} \mathcal{V}_+(x) &= \mathcal{V}_{+,0}(x) - \sqrt{\frac{\hbar Z_0}{4\pi}} \sum_{m=1}^N \sum_{j,j'} \pi \omega_{m,j'} G_m C_{m,j'} \\ &\times \sigma_{m,jj'} (\theta_H(x-x_m) e^{ik_{\omega_d}(x-x_m)} + e^{ik_{\omega_d}(x+x_m)}), \end{aligned} \quad (\text{D8a})$$

$$\begin{aligned} \mathcal{V}_-(x) &= \mathcal{V}_{-,0}(x) - \sqrt{\frac{\hbar Z_0}{4\pi}} \sum_{m=1}^N \sum_{j,j'} \pi \omega_{m,j'} G_m C_{m,j'} \\ &\times \sigma_{m,jj'} \theta_H(x_m-x) e^{ik_{\omega_d}(x_m-x)}. \end{aligned} \quad (\text{D8b})$$

The reflection coefficient is defined to be

$$r = \frac{\text{tr}[\mathcal{V}_+(x_N^+) \rho]}{\text{tr}[\mathcal{V}_-(x_N^+) \rho]}, \quad (\text{D9})$$

where $x_N^+ = x_N + \epsilon$ with $\epsilon > 0$ such that $\epsilon \rightarrow 0$ at the end of the calculation. We assume that the positions x_m are ordered such that they increase with increasing m , and hence x_N^+ is the position just to the right of the last subsystem attached to the transmission line. Hence, $\mathcal{V}_-(x_N^+) = \mathcal{V}_{-,0}(x_N^+)$. Using Eq. (A23), noting that due to Eq. (A26), we have $\text{tr}[\sigma_{m,jj'} \rho] = \text{tr}_s[\sigma_{m,jj'} \tilde{\rho}_s] e^{-i\omega_d t}$, and removing the overall propagation phase $e^{2ik_{\omega_d} x_N^+}$, the reflection coefficient

$$\begin{aligned} r &= 1 - i \sum_{m=1}^N \sum_{j,j'} \frac{\omega_{m,j'} \sqrt{\Gamma_m}}{\sqrt{\omega_d \omega_m}} \sqrt{\frac{\Gamma_m}{\dot{n}}} C_{m,jj'} \\ &\times \text{tr}_s[\sigma_{m,jj'} \tilde{\rho}_s] \cos(k_{\omega_d} x_m) e^{-i\phi} \end{aligned} \quad (\text{D10})$$

is obtained. Writing the photon flux \dot{n} in terms of the reference Rabi frequency Ω_1 using Eq. (12) with $x_1=0$, results in the expression (26) of the main text.

APPENDIX E: CALCULATION OF THE GRADIENT

In this Appendix, we give details about the calculation of the gradient for the optimal control approach used in Sec. V of the main text. The master equation (17) is rewritten such that the elements of the density matrix $\tilde{\rho}_s$ are arranged as a vector $\vec{\rho}_s$, resulting in $\dot{\vec{\rho}}_s = L(t)\vec{\rho}_s$. In the same way, the matrices $M_{\tilde{F}} = UAU^\dagger$ and $\rho_s(t) = \mathcal{M}(A)$ in Eq. (29) are also written as vectors $\vec{M}_{\tilde{F}}$ and $\vec{\rho}_s(t)$, and hence we can write Eq. (29) as the inner product

$$\tilde{F} = \vec{M}_{\tilde{F}}^\dagger \vec{\rho}_s(t), \quad (\text{E1})$$

where we have used the fact that $M_{\tilde{F}}$ is a Hermitian matrix. The latter follows from A either being a density matrix or one of the Pauli matrices, and U being unitary.

We solve the master equation with the fourth-order Runge-Kutta method and use the reverse mode automatic differentiation to calculate the gradient of Eq. (E1) with respect to the Fourier amplitudes a_p and b_p in the pulse shape parametrization (31). The gradient of the average fidelity (28) is then obtained by adding the contributions for all the initial matrices. Compared to the general case of the nonlinear differential equations solved by the Runge-Kutta method [57,58], the linearity of the master equation allows for an approach that is superficially similar to the other optimal control approaches where forward propagation of the equations of motion is alternated with backward propagation of the adjoint equations [59,60]. In contrast to Refs. [59,60], however, the derivation of the adjoint equation is more involved than simply taking the adjoint of $L(t)$.

Defining $\Delta t = t_f/N_t$, $t_n = (\Delta t)n$, $\vec{\rho}_n = \vec{\rho}_s(t_n)$, $L_{1,n} = L(t_n)\Delta t$, $L_{2,n} = L(t_n + (\Delta t)/2)\Delta t$, $L_{3,n} = L(t_{n+1})\Delta t$, the

fourth-order Runge-Kutta method can be written

$$\vec{k}_{1,n} = L_{1,n}\vec{\rho}_n, \quad (\text{E2a})$$

$$\vec{k}_{2,n} = L_{2,n}(\vec{\rho}_n + \vec{k}_{1,n}/2), \quad (\text{E2b})$$

$$\vec{k}_{3,n} = L_{2,n}(\vec{\rho}_n + \vec{k}_{2,n}/2), \quad (\text{E2c})$$

$$\vec{k}_{4,n} = L_{3,n}(\vec{\rho}_n + \vec{k}_{3,n}), \quad (\text{E2d})$$

$$\vec{\rho}_{n+1} = \vec{\rho}_n + \vec{k}_{1,n}/6 + \vec{k}_{2,n}/3 + \vec{k}_{3,n}/3 + \vec{k}_{4,n}/6. \quad (\text{E2e})$$

The reverse mode automatic differentiation applied to this algorithm requires storing or recomputing (during the backward propagation) the vectors $\vec{\rho}_n$, $\vec{k}_{1,n}$, $\vec{k}_{2,n}$, $\vec{k}_{3,n}$, and $\vec{k}_{4,n}$ for all n . The vectors $\vec{\rho}_n$ can be recomputed after the forward propagation by applying the Runge-Kutta method backward in time, starting from $\vec{\rho}_{N_t}$. In our numerical simulations, we store as many of the vectors $\vec{\rho}_n$ as could be fit into memory, uniformly spaced over all the time indices n . The vectors $\vec{\rho}_n$ between the stored ones are recomputed by applying the Runge-Kutta method backward in time. We find that this decreases the numerical error due to inexact recomputation of the vectors $\vec{\rho}_n$.

The vectors $\vec{k}_{1,n}$, $\vec{k}_{2,n}$, $\vec{k}_{3,n}$, and $\vec{k}_{4,n}$ are always recomputed but in an indirect way. We rewrite Eqs. (E2) into the form

$$\vec{\rho}_{n+1} = K_n \vec{\rho}_n, \quad (\text{E3})$$

where

$$\begin{aligned} K_n = & I + \frac{1}{6}L_{1,n} + \frac{1}{3}(L_{2,n} + \frac{1}{2}L_{2,n}L_{1,n}) + \frac{1}{3}L_{2,n} \\ & + \frac{1}{2}L_{2,n}L_{2,n} + \frac{1}{4}L_{2,n}L_{2,n}L_{1,n}) + \frac{1}{6}(L_{3,n} + L_{3,n}L_{2,n} \\ & + \frac{1}{2}L_{3,n}L_{2,n}L_{2,n} + \frac{1}{4}L_{3,n}L_{2,n}L_{2,n}L_{1,n}), \end{aligned} \quad (\text{E4})$$

and apply the reverse mode automatic differentiation on this form.

The gradient of Eq. (E1) at the final time $t = t_f$ is

$$\frac{\partial \vec{F}}{\partial a_p} = \vec{M}_F^\dagger \frac{\partial \vec{\rho}_{N_t}}{\partial a_p}, \quad \frac{\partial \vec{F}}{\partial b_p} = \vec{M}_F^\dagger \frac{\partial \vec{\rho}_{N_t}}{\partial b_p}, \quad (\text{E5})$$

where

$$\frac{\partial \vec{\rho}_n}{\partial a_p} = \frac{\partial K_{n-1}}{\partial a_p} \vec{\rho}_{n-1} + K_{n-1} \frac{\partial \vec{\rho}_{n-1}}{\partial a_p}, \quad (\text{E6a})$$

$$\frac{\partial \vec{\rho}_n}{\partial b_p} = \frac{\partial K_{n-1}}{\partial b_p} \vec{\rho}_{n-1} + K_{n-1} \frac{\partial \vec{\rho}_{n-1}}{\partial b_p}. \quad (\text{E6b})$$

By substituting these equations into themselves for all n and defining the initial value $\vec{\chi}_{N_t}^\dagger = \vec{M}_F^\dagger$ and the adjoint equation

$$\vec{\chi}_{n-1}^\dagger = \vec{\chi}_n^\dagger K_{n-1}, \quad (\text{E7})$$

we end up with

$$\frac{\partial \vec{F}}{\partial a_p} = \sum_{n=1}^{N_t} \vec{\chi}_n^\dagger \frac{\partial K_{n-1}}{\partial a_p} \vec{\rho}_{n-1}, \quad (\text{E8a})$$

$$\frac{\partial \vec{F}}{\partial b_p} = \sum_{n=1}^{N_t} \vec{\chi}_n^\dagger \frac{\partial K_{n-1}}{\partial b_p} \vec{\rho}_{n-1}, \quad (\text{E8b})$$

where the sums are can be efficiently evaluated by starting with $n = N_t$ and propagating $\vec{\chi}_n$ backward using Eq. (E7). We give more details below, but first we summarize the entire procedure:

(1) Propagate forward using Eqs. (E2), saving as many of the intermediate values $\vec{\rho}_n$, as can be fit into memory.

(2) Initialize $n = N_t$, and use $\vec{\chi}_{N_t}^\dagger = \vec{M}_F^\dagger$.

(3) If $\vec{\rho}_{n-1}$ is not stored in memory, calculate it by propagating Eqs. (E2) backward in time, otherwise use the stored $\vec{\rho}_{n-1}$.

(4) Evaluate the scalars given by Eqs. (E12).

(5) Add the contributions from this n to the gradient using Eqs. (E13) for all a_p and b_p .

(6) Calculate $\vec{\chi}_{n-1}$ using Eq. (E15).

(7) If $n > 0$, go to step 3 replacing n with $n - 1$. Otherwise, stop.

The above procedure needs a constant number of the computationally expensive matrix-vector multiplications for every time index n , independent of the number of the parameters a_p and b_p .

To derive the expressions for the above procedure, we first note that

$$(\Delta t) \frac{\partial L(t)}{\partial a_p} = \frac{\partial \text{Re}[\Omega]}{\partial a_p}(t) T_{\text{Re}}, \quad (\text{E9a})$$

$$(\Delta t) \frac{\partial L(t)}{\partial b_p} = \frac{\partial \text{Im}[\Omega]}{\partial b_p}(t) T_{\text{Im}}, \quad (\text{E9b})$$

where, assuming that the density matrix is written as a vector in the row-major form [i.e., $(\vec{\rho}_s)_{l,l'} = (\vec{\rho}_s)_{lN_b+l'}$, N_b is the Hilbert space basis size, and $0 \leq l, l' \leq N_b - 1$],

$$T_{\text{Re}} = -\frac{i}{\hbar} (\Delta t) (\vec{H}_{d,\text{Re}} \otimes I - I \otimes \vec{H}_{d,\text{Re}}^T), \quad (\text{E10a})$$

$$T_{\text{Im}} = -\frac{i}{\hbar} (\Delta t) (\vec{H}_{d,\text{Im}} \otimes I - I \otimes \vec{H}_{d,\text{Im}}^T), \quad (\text{E10b})$$

and $\vec{H}_{d,\text{Re}}$, $\vec{H}_{d,\text{Im}}$ are given by Eqs. (16). We define the following temporary vectors

$$\vec{l}_{0,n} = T_{\text{Re}} \vec{\rho}_n, \quad \vec{l}_{1,n} = L_{1,n} \vec{\rho}_n, \quad (\text{E11a})$$

$$\vec{l}_{2,n} = L_{2,n} \vec{\rho}_n, \quad \vec{l}_{3,n} = T_{\text{Re}} \vec{l}_{1,n}, \quad (\text{E11b})$$

$$\vec{l}_{4,n} = T_{\text{Re}} \vec{l}_{2,n}, \quad \vec{l}_{5,n} = L_{2,n} \vec{l}_{0,n}, \quad (\text{E11c})$$

$$\vec{l}_{6,n} = L_{2,n} \vec{l}_{1,n}, \quad \vec{l}_{7,n} = L_{2,n} \vec{l}_{3,n}, \quad (\text{E11d})$$

$$\vec{l}_{8,n} = L_{2,n} \vec{l}_{5,n}, \quad \vec{l}_{9,n} = T_{\text{Re}} \vec{l}_{6,n}; \quad (\text{E11e})$$

$$\vec{m}_{0,n} = T_{\text{Im}} \vec{\rho}_n, \quad \vec{m}_{1,n} = L_{1,n} \vec{\rho}_n, \quad (\text{E11f})$$

$$\vec{m}_{2,n} = L_{2,n} \vec{\rho}_n, \quad \vec{m}_{3,n} = T_{\text{Im}} \vec{m}_{1,n}, \quad (\text{E11g})$$

$$\vec{m}_{4,n} = T_{\text{Im}} \vec{m}_{2,n}, \quad \vec{m}_{5,n} = L_{2,n} \vec{m}_{0,n}, \quad (\text{E11h})$$

$$\vec{m}_{6,n} = L_{2,n} \vec{m}_{1,n}, \quad \vec{m}_{7,n} = L_{2,n} \vec{m}_{3,n}, \quad (\text{E11i})$$

$$\vec{m}_{8,n} = L_{2,n} \vec{m}_{5,n}, \quad \vec{m}_{9,n} = T_{\text{Im}} \vec{m}_{6,n}; \quad (\text{E11j})$$

and scalars

$$S_{1,n,\text{Re}} = \bar{\chi}_n^\dagger \left(\frac{1}{6} \bar{l}_{0,n-1} + \frac{1}{6} \bar{l}_{5,n-1} + \frac{1}{12} \bar{l}_{8,n-1} + \frac{1}{24} L_{3,n-1} \bar{l}_{8,n-1} \right), \quad (\text{E12a})$$

$$S_{2,n,\text{Re}} = \bar{\chi}_n^\dagger \left(\frac{2}{3} \bar{l}_{0,n-1} + \frac{1}{6} \bar{l}_{3,n-1} + \frac{1}{6} \bar{l}_{4,n-1} + \frac{1}{6} \bar{l}_{5,n-1} + \frac{1}{12} \bar{l}_{9,n-1} + \frac{1}{12} \bar{l}_{7,n-1} \right. \\ \left. + \frac{1}{6} L_{3,n-1} \left(\bar{l}_{0,n-1} + \frac{1}{2} \bar{l}_{4,n-1} + \frac{1}{2} \bar{l}_{5,n-1} + \frac{1}{4} \bar{l}_{9,n-1} + \frac{1}{4} \bar{l}_{7,n-1} \right) \right), \quad (\text{E12b})$$

$$S_{3,n,\text{Re}} = \bar{\chi}_n^\dagger \left(\frac{1}{6} \bar{l}_{0,n-1} + \frac{1}{6} \bar{l}_{4,n-1} + \frac{1}{12} T_{\text{Re}} L_{2,n-1} \left(\bar{l}_{2,n-1} + \frac{1}{2} \bar{l}_{6,n-1} \right) \right), \quad (\text{E12c})$$

$$S_{1,n,\text{Im}} = \bar{\chi}_n^\dagger \left(\frac{1}{6} \bar{m}_{0,n-1} + \frac{1}{6} \bar{m}_{5,n-1} + \frac{1}{12} \bar{m}_{8,n-1} + \frac{1}{24} L_{3,n-1} \bar{m}_{8,n-1} \right), \quad (\text{E12d})$$

$$S_{2,n,\text{Im}} = \bar{\chi}_n^\dagger \left(\frac{2}{3} \bar{m}_{0,n-1} + \frac{1}{6} \bar{m}_{3,n-1} + \frac{1}{6} \bar{m}_{4,n-1} + \frac{1}{6} \bar{m}_{5,n-1} + \frac{1}{12} \bar{m}_{9,n-1} + \frac{1}{12} \bar{m}_{7,n-1} \right. \\ \left. + \frac{1}{6} L_{3,n-1} \left(\bar{m}_{0,n-1} + \frac{1}{2} \bar{m}_{4,n-1} + \frac{1}{2} \bar{m}_{5,n-1} + \frac{1}{4} \bar{m}_{9,n-1} + \frac{1}{4} \bar{m}_{7,n-1} \right) \right), \quad (\text{E12e})$$

$$S_{3,n,\text{Im}} = \bar{\chi}_n^\dagger \left(\frac{1}{6} \bar{m}_{0,n-1} + \frac{1}{6} \bar{m}_{4,n-1} + \frac{1}{12} T_{\text{Re}} L_{2,n-1} \left(\bar{m}_{2,n-1} + \frac{1}{2} \bar{m}_{6,n-1} \right) \right). \quad (\text{E12f})$$

The above definitions allow us to write

$$\bar{\chi}_n^\dagger \frac{\partial K_{n-1}}{\partial a_p} \bar{\rho}_{n-1} = \frac{\partial \text{Re}[\Omega]}{\partial a_p} (t_{n-1}) S_{1,n,\text{Re}} \\ + \frac{\partial \text{Re}[\Omega]}{\partial a_p} (t_{n-1} + (\Delta t)/2) S_{2,n,\text{Re}} \\ + \frac{\partial \text{Re}[\Omega]}{\partial a_p} (t_n) S_{3,n,\text{Re}}, \quad (\text{E13a})$$

$$\bar{\chi}_n^\dagger \frac{\partial K_{n-1}}{\partial b_p} \bar{\rho}_{n-1} = \frac{\partial \text{Im}[\Omega]}{\partial b_p} (t_{n-1}) S_{1,n,\text{Im}} \\ + \frac{\partial \text{Im}[\Omega]}{\partial b_p} (t_{n-1} + (\Delta t)/2) S_{2,n,\text{Im}} \\ + \frac{\partial \text{Im}[\Omega]}{\partial b_p} (t_n) S_{3,n,\text{Im}}. \quad (\text{E13b})$$

The backward propagation in Eq. (E7) can also be written explicitly. Define

$$\bar{\mu}_{1,n} = L_{2,n-1}^\dagger \bar{\chi}_n, \quad \bar{\mu}_{2,n} = L_{3,n-1}^\dagger \bar{\chi}_n, \quad (\text{E14a})$$

$$\bar{\mu}_{3,n} = L_{2,n-1}^\dagger \bar{\mu}_{1,n}, \quad \bar{\mu}_{4,n} = L_{2,n-1}^\dagger \bar{\mu}_{2,n}, \quad (\text{E14b})$$

$$\bar{\mu}_{5,n} = L_{2,n-1}^\dagger \bar{\mu}_{4,n}. \quad (\text{E14c})$$

Then

$$\bar{\chi}_{n-1} = \bar{\chi}_n + L_{1,n-1}^\dagger \left(\frac{1}{6} \bar{\chi}_n + \frac{1}{6} \bar{\mu}_{1,n} + \frac{1}{12} \bar{\mu}_{3,n} + \frac{1}{24} \bar{\mu}_{5,n} \right) \\ + \frac{2}{3} \bar{\mu}_{1,n} + \frac{1}{6} \bar{\mu}_{2,n} + \frac{1}{6} \bar{\mu}_{3,n} + \frac{1}{6} \bar{\mu}_{4,n} + \frac{1}{12} \bar{\mu}_{5,n}. \quad (\text{E15})$$

-
- [1] F. Arute, K. Arya, R. Babbush, D. Bacon, J. C. Bardin, R. Barends, R. Biswas, S. Boixo, F. G. S. L. Brandao, D. A. Buell *et al.*, Quantum supremacy using a programmable superconducting processor, *Nature (London)* **574**, 505 (2019).
- [2] P. Jurcevic, A. Javadi-Abhari, L. S. Bishop, I. Lauer, D. F. Bogorin, M. Brink, L. Capelluto, O. Günlük, T. Itoko, N. Kanazawa *et al.*, Demonstration of quantum volume 64 on a superconducting quantum computing system, *Quantum Sci. Technol.* **6**, 025020 (2021).
- [3] M. Gong, S. Wang, C. Zha, M.-C. Chen, H.-L. Huang, Y. Wu, Q. Zhu, Y. Zhao, S. Li, S. Guo *et al.*, Quantum walks on a programmable two-dimensional 62-qubit superconducting processor, *Science* **372**, 948 (2021).
- [4] Q. Zhu, S. Cao, F. Chen, M.-C. Chen, X. Chen, T.-H. Chung, H. Deng, Y. Du, D. Fan, M. Gong *et al.*, Quantum computational advantage via 60-qubit 24-cycle random circuit sampling, *Sci. Bull.* **67**, 240 (2022).
- [5] E. J. Zhang, S. Srinivasan, N. Sundaresan, D. F. Bogorin, Y. Martin, J. B. Hertzberg, J. Timmerwille, E. J. Pritchett, J.-B. Yau, C. Wang *et al.*, High-performance superconducting quantum processors via laser annealing of transmon qubits, *Sci. Adv.* **8**, eabif6690 (2022).
- [6] E. H. Chen, T. J. Yoder, Y. Kim, N. Sundaresan, S. Srinivasan, M. Li, A. D. Córcoles, A. W. Cross, and M. Takita, Calibrated Decoders for Experimental Quantum Error Correction, *Phys. Rev. Lett.* **128**, 110504 (2022).
- [7] Y. Zhao, Y. Ye, H.-L. Huang, Y. Zhang, D. Wu, H. Guan, Q. Zhu, Z. Wei, T. He, S. Cao, F. Chen, T.-H. Chung, H. Deng, D. Fan, M. Gong, C. Guo, S. Guo, L. Han, N. Li, S. Li *et al.*, Realization of an Error-Correcting Surface Code with Superconducting Qubits, *Phys. Rev. Lett.* **129**, 030501 (2022).
- [8] R. Acharya, I. Aleiner, R. Allen, T. I. Andersen, M. Ansmann, F. Arute, K. Arya, A. Asfaw, J. Atalaya, R. Babbush *et al.*, Suppressing quantum errors by scaling a surface code logical qubit, [arXiv:2207.06431](https://arxiv.org/abs/2207.06431).
- [9] M. D. Reed, B. R. Johnson, A. A. Houck, L. DiCarlo, J. M. Chow, D. I. Schuster, L. Frunzio, and R. J. Schoelkopf, Fast reset and suppressing spontaneous emission of a superconducting qubit, *Appl. Phys. Lett.* **96**, 203110 (2010).
- [10] E. Jeffrey, D. Sank, J. Y. Mutus, T. C. White, J. Kelly, R. Barends, Y. Chen, Z. Chen, B. Chiaro, A. Dunsworth, A. Megrant, P. J. J. O'Malley, C. Neill, P. Roushan, A. Vainsencher, J. Wenner, A. N. Cleland, and J. M. Martinis, Fast Accurate State Measurement with Superconducting Qubits, *Phys. Rev. Lett.* **112**, 190504 (2014).

- [11] N. T. Bronn, Y. Liu, J. B. Hertzberg, A. D. Córcoles, A. A. Houck, J. M. Gambetta, and J. M. Chow, Broadband filters for abatement of spontaneous emission in circuit quantum electrodynamics, *Appl. Phys. Lett.* **107**, 172601 (2015).
- [12] Y. Sunada, S. Kono, J. Iives, S. Tamate, T. Sugiyama, Y. Tabuchi, and Y. Nakamura, Fast Readout and Reset of a Superconducting Qubit Coupled to a Resonator with an Intrinsic Purcell Filter, *Phys. Rev. Appl.* **17**, 044016 (2022).
- [13] K. Koshino, S. Kono, and Y. Nakamura, Protection of a Qubit via Subradiance: A Josephson Quantum Filter, *Phys. Rev. Appl.* **13**, 014051 (2020).
- [14] S. Kono, K. Koshino, D. Lachance-Quirion, A. F. van Loo, Y. Tabuchi, A. Noguchi, and Y. Nakamura, Breaking the trade-off between fast control and long lifetime of a superconducting qubit, *Nat. Commun.* **11**, 3683 (2020).
- [15] M. Jerger, S. Poletto, P. Macha, U. Hübner, E. Il'ichev, and A. V. Ustinov, Frequency division multiplexing readout and simultaneous manipulation of an array of flux qubits, *Appl. Phys. Lett.* **101**, 042604 (2012).
- [16] Y. Chen, D. Sank, P. O'Malley, T. White, R. Barends, B. Chiaro, J. Kelly, E. Lucero, M. Mariantoni, A. Megrant, C. Neill, A. Vainsencher, J. Wenner, Y. Yin, A. N. Cleland, and J. M. Martinis, Multiplexed dispersive readout of superconducting phase qubits, *Appl. Phys. Lett.* **101**, 182601 (2012).
- [17] D. Rosenberg, D. Kim, R. Das, D. Yost, S. Gustavsson, D. Hover, P. Krantz, A. Melville, L. Racz, G. O. Samach, S. J. Weber, F. Yan, J. L. Yoder, A. J. Kerman, and W. D. Oliver, 3D integrated superconducting qubits, *npj Quantum Inf.* **3**, 42 (2017).
- [18] D. Lachance-Quirion, S. P. Wolski, Y. Tabuchi, S. Kono, K. Usami, and Y. Nakamura, Entanglement-based single-shot detection of a single magnon with a superconducting qubit, *Science* **367**, 425 (2020).
- [19] A. A. Houck, J. A. Schreier, B. R. Johnson, J. M. Chow, J. Koch, J. M. Gambetta, D. I. Schuster, L. Frunzio, M. H. Devoret, S. M. Girvin, and R. J. Schoelkopf, Controlling the Spontaneous Emission of a Superconducting Transmon Qubit, *Phys. Rev. Lett.* **101**, 080502 (2008).
- [20] M. Malekakhlagh and H. E. Türeci, Origin and implications of an A^2 -like contribution in the quantization of circuit-QED systems, *Phys. Rev. A* **93**, 012120 (2016).
- [21] M. Malekakhlagh, A. Petrescu, and H. E. Türeci, Cutoff-Free Circuit Quantum Electrodynamics, *Phys. Rev. Lett.* **119**, 073601 (2017).
- [22] M. F. Gely, A. Parra-Rodríguez, D. Bothner, Y. M. Blanter, S. J. Bosman, E. Solano, and G. A. Steele, Convergence of the multi-mode quantum Rabi model of circuit quantum electrodynamics, *Phys. Rev. B* **95**, 245115 (2017).
- [23] M. Bamba and T. Ogawa, Recipe for the Hamiltonian of system-environment coupling applicable to the ultrastrong-light-matter-interaction regime, *Phys. Rev. A* **89**, 023817 (2014).
- [24] J. R. Ott, M. Wubs, P. Lodahl, N. A. Mortensen, and R. Kaiser, Cooperative fluorescence from a strongly driven dilute cloud of atoms, *Phys. Rev. A* **87**, 061801(R) (2013).
- [25] R. H. Lehberg, Radiation from an N -atom system. I. General formalism, *Phys. Rev. A* **2**, 883 (1970).
- [26] K. Wódkiewicz and J. Eberly, Markovian and non-Markovian behavior in two-level atom fluorescence, *Ann. Phys.* **101**, 574 (1976).
- [27] I. de Vega and D. Alonso, Dynamics of non-Markovian open quantum systems, *Rev. Mod. Phys.* **89**, 015001 (2017).
- [28] J. M. Gambetta, Control of Superconducting Qubits, in *Quantum Information Processing Lecture Notes*, 44th IFF Spring School 2013 (2013).
- [29] J. J. Burnett, A. Bengtsson, M. Scigliuzzo, D. Niepce, M. Kudra, P. Delsing, and J. Bylander, Decoherence benchmarking of superconducting qubits, *npj Quantum Inf.* **5**, 54 (2019).
- [30] A. P. M. Place, L. V. H. Rodgers, P. Mundada, B. M. Smitham, M. Fitzpatrick, Z. Leng, A. Premkumar, J. Bryon, A. Vrajitoarea, S. Sussman *et al.*, New material platform for superconducting transmon qubits with coherence times exceeding 0.3 milliseconds, *Nat. Commun.* **12**, 1779 (2021).
- [31] C. Wang, X. Li, H. Xu, Z. Li, J. Wang, Z. Yang, Z. Mi, X. Liang, T. Su, C. Yang *et al.*, Towards practical quantum computers: Transmon qubit with a lifetime approaching 0.5 milliseconds, *npj Quantum Inf.* **8**, 3 (2022).
- [32] A. A. Clerk, M. H. Devoret, S. M. Girvin, F. Marquardt, and R. J. Schoelkopf, Introduction to quantum noise, measurement, and amplification, *Rev. Mod. Phys.* **82**, 1155 (2010).
- [33] M. Naghiloo, Introduction to experimental quantum measurement with superconducting qubits, [arXiv:1904.09291](https://arxiv.org/abs/1904.09291).
- [34] L. Stefanazzi, K. Treptow, N. Wilcer, C. Stoughton, C. Bradford, S. Uemura, S. Zorzetti, S. Montella, G. Cancelo, S. Sussman *et al.*, The QICK (Quantum Instrumentation Control Kit): Readout and control for qubits and detectors, *Rev. Sci. Instrum.* **93**, 044709 (2022).
- [35] M. O. Tholén, R. Borgani, G. R. Di Carlo, A. Bengtsson, C. Križan, M. Kudra, G. Tancredi, J. Bylander, P. Delsing, S. Gasparinetti, and D. B. Haviland, Measurement and control of a superconducting quantum processor with a fully integrated radio-frequency system on a chip, *Rev. Sci. Instrum.* **93**, 104711 (2022).
- [36] J. Gambetta, W. A. Braff, A. Wallraff, S. M. Girvin, and R. J. Schoelkopf, Protocols for optimal readout of qubits using a continuous quantum nondemolition measurement, *Phys. Rev. A* **76**, 012325 (2007).
- [37] H. M. Wiseman and G. J. Milburn, *Quantum Measurement and Control* (Cambridge University Press, Cambridge, 2009).
- [38] D. T. Sank, Fast, Accurate State Measurement in Superconducting Qubits, Ph.D. thesis, University of California, Santa Barbara, 2014.
- [39] M. J. D. Powell, The BOBYQA Algorithm for Bound Constrained Optimization without Derivatives, Tech. Rep. NA2009/06 (Department of Applied Mathematics and Theoretical Physics, Cambridge, 2009).
- [40] S. G. Johnson, The NLOpt nonlinear-optimization package. <https://github.com/stevengj/nlopt>
- [41] J. Y. Mutus, T. C. White, R. Barends, Y. Chen, Z. Chen, B. Chiaro, A. Dunsworth, E. Jeffrey, J. Kelly, A. Megrant *et al.*, Strong environmental coupling in a Josephson parametric amplifier, *Appl. Phys. Lett.* **104**, 263513 (2014).
- [42] S. Masuda and K. Koshino, Effects of higher levels of qubits on control of qubit protected by a Josephson quantum filter, *New J. Phys.* **23**, 013006 (2021).
- [43] F. Motzoi, J. M. Gambetta, P. Rebentrost, and F. K. Wilhelm, Simple Pulses for Elimination of Leakage in Weakly Nonlinear Qubits, *Phys. Rev. Lett.* **103**, 110501 (2009).

- [44] P. Doria, T. Calarco, and S. Montangero, Optimal Control Technique for Many-Body Quantum Dynamics, *Phys. Rev. Lett.* **106**, 190501 (2011).
- [45] F. Motzoi, J. M. Gambetta, S. T. Merkel, and F. K. Wilhelm, Optimal control methods for rapidly time-varying Hamiltonians, *Phys. Rev. A* **84**, 022307 (2011).
- [46] M. D. Bowdrey, D. K. Oi, A. Short, K. Banaszek, and J. Jones, Fidelity of single qubit maps, *Phys. Lett. A* **294**, 258 (2002).
- [47] M. A. Nielsen, A simple formula for the average gate fidelity of a quantum dynamical operation, *Phys. Lett. A* **303**, 249 (2002).
- [48] J. Nocedal, Updating quasi-Newton matrices with limited storage, *Math. Comput.* **35**, 773 (1980).
- [49] W. D. Kalfus, D. F. Lee, G. J. Ribeill, S. D. Fallek, A. Wagner, B. Donovan, D. Ristè, and T. A. Ohki, High-fidelity control of superconducting qubits using direct microwave synthesis in higher Nyquist zones, *IEEE Trans. Quantum Eng.* **1**, 1 (2020).
- [50] M. Abdelhafez, D. I. Schuster, and J. Koch, Gradient-based optimal control of open quantum systems using quantum trajectories and automatic differentiation, *Phys. Rev. A* **99**, 052327 (2019).
- [51] M. Werninghaus, D. J. Egger, F. Roy, S. Machnes, F. K. Wilhelm, and S. Filipp, Leakage reduction in fast superconducting qubit gates via optimal control, *npj Quantum Inf.* **7**, 14 (2021).
- [52] B. Davies and B. Martin, Numerical inversion of the Laplace transform: A survey and comparison of methods, *J. Comput. Phys.* **33**, 1 (1979).
- [53] D. G. Duffy, On the numerical inversion of Laplace transforms: Comparison of three new methods on characteristic problems from applications, *ACM Trans. Math. Softw.* **19**, 333 (1993).
- [54] K. L. Kuhlman, Review of inverse Laplace transform algorithms for Laplace-space numerical approaches, *Numer. Alg.* **63**, 339 (2013).
- [55] K. J. Blow, R. Loudon, S. J. D. Phoenix, and T. J. Shepherd, Continuum fields in quantum optics, *Phys. Rev. A* **42**, 4102 (1990).
- [56] H. J. Oberle and H. J. Pesch, Numerical treatment of delay differential equations by Hermite Interpolation, *Numer. Math.* **37**, 235 (1981).
- [57] Y. Evtushenko, Computation of exact gradients in distributed dynamic systems, *Optim. Methods Software* **9**, 45 (1998).
- [58] A. Walther, Automatic differentiation of explicit Runge-Kutta methods for optimal control, *Comput. Optim. Appl.* **36**, 83 (2007).
- [59] R. Kosloff, S. Rice, P. Gaspard, S. Tersigni, and D. Tannor, Wavepacket dancing: Achieving chemical selectivity by shaping light pulses, *Chem. Phys.* **139**, 201 (1989).
- [60] J. Somló, V. A. Kazakov, and D. J. Tannor, Controlled dissociation of I_2 via optical transitions between the X and B electronic states, *Chem. Phys.* **172**, 85 (1993).